

Atomic layer deposition of complex thin films

Esko Ahvenniemi

Atomic layer deposition of complex thin films

Esko Ahvenniemi

A doctoral dissertation completed for the degree of Doctor of Science (Technology) to be defended, with the permission of the Aalto University School of Chemical Technology, at a public examination held at the lecture hall Ke2 of the school on 25th of November 2016 at 12.

**Aalto University
School of Chemical Technology
Department of Chemistry
Laboratory of Inorganic Chemistry**

Supervising professor

Professor Maarit Karppinen

Preliminary examiners

Ph.D. Ville Miikkulainen, University of Helsinki, Finland

Associate Professor Henrik Pedersen, Linköping University, Sweden

Opponent

Professor Christophe Detavernier, Ghent University, Belgium

Aalto University publication series

DOCTORAL DISSERTATIONS 215/2016

© Esko Ahvenniemi

ISBN 978-952-60-7080-3 (printed)

ISBN 978-952-60-7079-7 (pdf)

ISSN-L 1799-4934

ISSN 1799-4934 (printed)

ISSN 1799-4942 (pdf)

<http://urn.fi/URN:ISBN:978-952-60-7079-7>

Unigrafia Oy

Helsinki 2016

Finland



Author

Esko Ahvenniemi

Name of the doctoral dissertation

Atomic layer deposition of complex thin films

Publisher School of Chemical Technology

Unit Department of Chemistry

Series Aalto University publication series DOCTORAL DISSERTATIONS 215/2016

Field of research Inorganic Chemistry

Manuscript submitted 22 September 2016

Date of the defence 25 November 2016

Permission to publish granted (date) 5 October 2016

Language English

☐ **Monograph**

☒ **Article dissertation**

☐ **Essay dissertation**

Abstract

Atomic layer deposition (ALD) is an advanced method for fabricating thin films on various substrate chemistries and architectures. It is employed commercially in semiconductor industry where typically thin films of binary oxides are employed in high-tech devices. Simple binary films have many useful properties, but to exploit the whole potential of the nanoscale devices, studies on more complex materials are required. Ternary and quaternary compounds possess several potentially exciting properties, but so far the studies on these complex ALD-fabricated thin films have been relatively scarce.

Device thicknesses measured in nanometers can bring astonishing advantages for a number of frontier applications such as solid oxide fuel cells. For example, thin film cathodes benefit in massively lowered operation temperatures due to the exclusion of the bulk properties of the material. In this dissertation, ALD processes were developed for SrCoO_{3-d} and $(\text{La,Sr})\text{CoO}_{3-d}$ thin films to complete the set of ALD processes for one of the best cathode materials, $(\text{La,Sr})(\text{Co,Fe})\text{O}_{3-d}$, and to gain deeper understanding of the growth of complex oxide films in general.

Moreover, the dissertation studies concerned a relatively new class of materials, i.e. hybrid atomic/molecular layer deposition (ALD/MLD) fabricated inorganic-organic hybrid thin films, where different metal cations and organic molecules are mixed together creating materials which combine the best properties from the both worlds. When this dissertation research was initiated, ALD/MLD processes had been developed only for Al, Ti and Zn metal constituents, and practically only diols has been used as organic constituents. In this dissertation, di- and tricarboxylic acids are presented as highly reactive organic precursors even with the stable but vastly applied β -diketonate precursors to deliver copper, cobalt, manganese and calcium based hybrid ALD/MLD thin films with exciting structural features.

Keywords Atomic layer deposition, atomic/molecular layer deposition, ternary, quaternary, hybrid, thin films

ISBN (printed) 978-952-60-7080-3

ISBN (pdf) 978-952-60-7079-7

ISSN-L 1799-4934

ISSN (printed) 1799-4934

ISSN (pdf) 1799-4942

Location of publisher Helsinki

Location of printing Helsinki

Year 2016

Pages 91

urn <http://urn.fi/URN:ISBN:978-952-60-7079-7>

Tekijä

Esko Ahvenniemi

Väitöskirjan nimi

Monimutkaiset ohutkalvot atomikerroskasvatusmenetelmällä

Julkaisija Kemian tekniikan korkeakoulu

Yksikkö Kemian laitos

Sarja Aalto University publication series DOCTORAL DISSERTATIONS 215/2016

Tutkimusala Epäorgaaninen kemia

Käsikirjoituksen pvm 22.09.2016

Väitöspäivä 25.11.2016

Julkaisuluvan myöntämispäivä 05.10.2016

Kieli Englanti

☐ **Monografia**

☒ **Artikkeliväitöskirja**

☐ **Esseeväitöskirja**

Tiivistelmä

Atomikerroskasvatus (atomic layer deposition, ALD) on kehittynyt ohutkalvojen kasvatusmenetelmä, joka ei ole juurikaan rajoittunut kasvatusalustan kemian tai arkkitehtuurin suhteen. Menetelmää käytetään puolijohdeteollisuudessa, jossa ohuet binääriset oksidikerrokset toimivat eristemateriaaleina korkean teknologian laitteissa. Yksinkertaisilla binäärisillä ohutkalvoilla on useita hyödyllisiä ominaisuuksia, mutta tarvitaan monimutkaisempia materiaaleja, jotta nanolaitteiden koko potentiaali voitaisiin ottaa hyötykäyttöön. Ternäärisillä ja kvaternäärisillä yhdisteillä on useita mielenkiintoisia ja hyödyllisiä ominaisuuksia, mutta tähän mennessä niiden tutkimus ALD-menetelmällä on ollut suhteellisen vähäistä.

Materiaalien ominaisuudet voivat parantua radikaalisti paksuuksien lähentyessä nanomittaluokkaa, kuten käy esimerkiksi kiinteäoksidipolito-kennoilla, joissa katodien valmistaminen nanometrikokoluokassa alentaa käyttölämpötilaa merkittävästi toimintahakkuuden parantuessa. Tässä väitöskirjatyössä kehitettiin ALD-prosessit SrCoO_{3-d} ja $(\text{La,Sr})\text{CoO}_{3-d}$ -materiaaleille, jotka täydensivät ALD-prosessien sarjan yhdelle lupaavimmalle katodimateriaalille $(\text{La,Sr})(\text{Co,Fe})\text{O}_{3-d}$ -lle. Lisäksi väitöstutkimuksessa pyrittiin ymmärtämään laajemmin monimutkaisten ohutkalvojen kasvatusa.

Väitöskirjatyössä perehdyttiin myös suhteellisen uuden ohutkalvomateriaaliluokan tutkimiseen, jossa valmistetaan epäorgaanis-organisia hybridimateriaaleja atomi/molekyylikerroskasvatuksella (ALD/MLD). Tällä menetelmällä metallikationit ja orgaaniset molekyylit muodostavat hybridimateriaaleja, joissa yhdistyy molempien materiaaliluokkien parhaita ominaisuuksia. Väitöstutkimuksen alussa ALD/MLD -prosesseja oli kehitetty vain alumiini-, titaani- ja sinkkimateriaaleille käytännössä ainoastaan diolien ollessa orgaanisena osana. Tässä väitöskirjatyössä, di- ja trikarboksyylihapot havaittiin reagoivan täydellisesti vakaiden, stabiilien ja paljon tutkittujen -diketonaattien kanssa. Lisäksi uusia hybridimateriaaleja valmistettiin kuparin, koboltin, mangaanin tai kalsiumin ollessa metallina, joilla havaittiin löytyvän uusia mielenkiintoisia rakenteellisia ominaisuuksia.

Avainsanat Atomikerroskasvatus, atomi-/molekyylikerroskasvatus, ternäärinen, kvaternäärinen, hybridi, ohutkalvot

ISBN (painettu) 978-952-60-7080-3

ISBN (pdf) 978-952-60-7079-7

ISSN-L 1799-4934

ISSN (painettu) 1799-4934

ISSN (pdf) 1799-4942

Julkaisupaikka Helsinki

Painopaikka Helsinki

Vuosi 2016

Sivumäärä 91

urn <http://urn.fi/URN:ISBN:978-952-60-7079-7>

Acknowledgements

The thesis work was carried out during five years between 2011 and 2016. Walter Ahlström Foundation and Tekniikan Edistämissäätiö are acknowledged for personal grants, and Scandinavia-Sasakawa Foundation for travel grant to visit the Institute for Solid State Physics of the University of Tokyo in Japan.

Professor Maarit Karppinen welcomed me into the research group and presented me the world of thin films and inorganic chemistry, of which I knew almost nothing from previous experience. She has listened to my wishes and helped me to overcome my barriers as an independent researcher in many ways by establishing a safe and high-profile research environment for us all. Thank you Maarit.

D.Sc. (Tech.) Mikko Matvejeff was the person which who helped me in the very beginning of my research career by learning ALD with me hands-on. It started with fixing the oddly-behaving MC reactor but in the end, after plenty of dead-ends, we got three joint publications and a lot of knowhow considering thin films. He also brought me to Japan to learn PLD in Prof. Mikk Lippmaa's group. Thank you Mikko for everything.

I've had the pleasure to have many skillful colleagues through my doctoral studies, from whom I have learned so much. Many of you have already gone to seek new opportunities all around the world, but luckily the new people have turned out to be awesome as well. The professional and the not-so-professional discussions and projects have made this worth it, including the Thin Solid Pancakes and the "great" movies every Thursday. Our pancake mafia has helped me to enjoy my time in the lab, but I'm not sure if I can say the same about the movies...

Finally, to my friends and family; thank you for being there all the time, every day. Thank you for the best (and worst) jokes, stories and memories. Special thanks must go to Kylli, who was an important detail in most of my ALD presentations and always happy to greet me at home.

It truly has been a journey.

Helsinki, 21st of September 2016

ESko Ahvenniemi

Contents

Acknowledgements.....	3
List of Abbreviations and Symbols.....	7
List of Publications.....	9
Author's Contribution.....	11
1. Introduction.....	12
2. Methodology.....	14
2.1. X-ray reflectivity (XRR).....	14
2.2. Grazing incidence X-ray diffraction (GIXRD).....	16
2.3. Fourier transform infrared (FTIR) spectroscopy.....	17
2.4. Physisorption measurements.....	18
2.5. Elongation measurements.....	19
3. Thin film depositions of complex oxide and hybrid materials..	22
3.1. Physical and chemical vapour deposited thin films.....	22
3.2. ALD of the binary oxides.....	22
3.2.1. The optimization of the ALD cycle.....	24
3.2.2. Precursors.....	25
3.3. ALD of the complex oxides.....	27
3.3.1. Ternary and quaternary oxides.....	27
3.3.2. The growth optimisation.....	28
3.3.3. Solid oxide fuel cell cathode materials.....	30
3.3.4. Case studies: $\text{SrCoO}_{3-\delta}$ and $(\text{La,Sr})\text{CoO}_{3-\delta}$	31
3.4. Hybrid atomic/molecular layer deposition.....	35
3.4.1. Case studies: Ca, Mn, Co and Cu based hybrid thin films	37
4. Conclusions.....	48
References.....	51

List of Abbreviations and Symbols

acac	Acetyl acetate
AFM	Atomic force microscopy
ALD	Atomic layer deposition
ALE	Atomic layer epitaxy
BET	Brunauer-Emmett-Teller
BJH	Barrett-Joyner-Halenda
CVD	Chemical vapour deposition
FTIR	Fourier transform infrared spectroscopy
GIXRD	Grazing incident X-ray diffraction
GPC	Growth per cycle
IT-SOFC	Intermediate temperature solid oxide fuel cell
ICP-OES	Inductive coupled plasma atomic emission spectroscopy
MIEC	Mixed ionic-electronic conductor
MLD	Molecular layer deposition
NLDFT	Nonlocal density function theory
PVD	Physical vapour deposition
SOFC	Solid oxide fuel cell
TEC	Thermal expansion coefficient
thd	2,2,6,6-tetramethyl-3,5-heptanedione
TP	Terephthalate
TPA	Terephthalic acid
XPS	X-ray photoelectron spectroscopy
XRF	X-ray fluorescence spectroscopy
XRR	X-ray reflectivity

List of Publications

This doctoral dissertation consists of a summary and of the following publications which are referred to in the text by their Roman numerals.

- I** E. Ahvenniemi, M. Matvejeff and M. Karppinen, SrCoO_{3-δ} thin films by atomic layer deposition, *Applied Surface Science* **320**, 838-842 (2014).
- II** E. Ahvenniemi, M. Matvejeff and M. Karppinen, Atomic layer deposition of quaternary oxide (La,Sr)CoO_{3-δ} thin films, *Dalton Transactions* **44**, 8001-8006 (2015).
- III** E. Ahvenniemi and M. Karppinen, Atomic/molecular layer deposition: a direct gas-phase route to crystalline metal-organic framework thin films, *Chemical Communications* **52**, 1139-1142 (2016).
- IV** E. Ahvenniemi and M. Karppinen, ALD/MLD processes for Mn and Co based hybrid thin films, *Dalton Transactions* **45**, 10730-10735 (2016).
- V** E. Ahvenniemi and M. Karppinen, In-situ atomic/molecular layer-by-layer deposition of inorganic-organic coordination network thin films from gaseous precursors, *Chemistry of Materials* **28**, 6260-6265 (2016).

Author's Contribution

Publication I: SrCoO_{3-δ} thin films by atomic layer deposition

The author defined the research plan with the co-authors and performed ca. 2/3 the depositions, thd-syntheses, results evaluations and the following characterizations: XRR, GIXRD, XRF, AFM, R-T, Seebeck measurements and FTIR. M.M conducted ca. 1/3 of the laboratory work. The author wrote the first draft of the manuscript and finalized the paper with M.M. and M.K.

Publication II: Atomic layer deposition of quaternary oxide (La,Sr)CoO_{3-δ} thin films

The author defined the research plan with the co-authors and performed ca. 4/5 of the depositions, thd-syntheses, results analyses and the following characterizations: XRR, GIXRD, XRF and FTIR. M.M. conducted ca. 1/5 of the laboratory work. The author wrote the first draft of the manuscript and finalized the paper with M.M. and M.K.

Publication III: Atomic/molecular layer deposition: a direct gas-phase route to crystalline metal-organic framework thin films

The author defined the research plan with M.K, performed all the depositions, thd-syntheses and the following characterizations: XRR, ellipsometry, GIXRD and FTIR. The author wrote the first draft of the manuscript and finalized the paper with M.K.

Publication IV: ALD/MLD processes for Mn and Co based hybrid thin films

The author defined the research plan with M.K., performed all the depositions, thd-syntheses and the following characterizations: XRR, GIXRD, AFM and FTIR. The author wrote the first draft of the manuscript and finalized the paper with M.K.

Publication V: In-situ atomic/molecular layer-by-layer deposition of inorganic-organic coordination network thin films from gaseous precursors

The author defined the research plan with M.K., performed all the depositions, thd-syntheses, results analyses and the following characterizations: XRR, GIXRD, AFM, FTIR and the elongation measurements. The author wrote the first draft of the manuscript and finalized the paper with M.K.

1. Introduction

The methods of producing ever diminutive and power efficient devices would have hit a brick wall without the invention of the atomic layer epitaxy (ALE) thin film deposition technique, invented and patented in the '70s by Suntola and Antson for manufacturing thin pinhole-free zinc sulphide layers for thin-film electroluminescent (TFEL) displays,¹ and also independently studied in USSR by Alekovskii et al. since the late 60s.^{2,3} Presently, the technique is most commonly called atomic layer deposition (ALD). It is in world-wide use e.g. in the fabrication of high quality dielectric films for efficient metal-oxide-semiconductor field effect transistors (MOSFET) and dynamic random access memories (DRAM).⁴ The semiconductor industry has been the main motivator in the development of the ALD method, as the other processing methods of depositing conformal, thin coatings over various types of substrates are scarce and prove certain difficulties in large scale production.⁵ The atomic level control of the films has become the main solution to the industry where the micro-fabrication processes appear to be the key limiting factor rather than the deposition of a few nanometer thick pinhole-free films.

The ALD of oxide materials has solutions for the deposition of a wide range of materials applicable e.g. for gas barrier materials, high- and low- κ dielectric materials, etch-stops, magnetic materials, transparent conducting oxides, thermoelectrics, cathodes, anodes or electrolytes in energy solutions and anti-reflection coatings. Some of the sought properties require complex materials with more than one cation species. Such properties include piezoelectrics, giant magnetoresistance devices, superconductors and metallic-type conductors, which can have outstanding performance with ternary/quaternary perovskite-type $\text{ABO}_{3-\delta}$ materials where A and B represent different cations.⁶⁻⁹ In addition to the perovskite-type materials, a slightly different type of complex ALD-type technique exists where an organic molecule with a reactive functional group is in a key role.^{10,11} The sequential introduction of organic species, similarly as the precursors in ALD processes, is called molecular layer deposition (MLD). The combination of ALD and MLD processes then yields hybrid inorganic-organic thin films, superlattice structures or nanolaminates, depending on the way of mixing the two methods.^{5,10} In hybrid ALD/MLD, the properties of both inorganic and organic worlds can be combined with the selection of ALD and MLD components, and the resulting hybrid thin films are usable e.g. in thermoelectrics, where the boundaries between the two materials scatter heat transferring

Table 1: Oxide and hybrid materials deposited with the ALD method arranged by the atomic number, where underlined species have β -diketonate precursors available.

Oxides^{6,12}
<p>Li, Be, B, <u>Mg</u>, Al, Si, P, <u>Ca</u>, <u>Sc</u>, Ti, <u>V</u>, <u>Cr</u>, <u>Mn</u>, <u>Fe</u>, <u>Co</u>, <u>Ni</u>, <u>Cu</u>, Zn, <u>Ga</u>, Ge, <u>Sr</u>, <u>Y</u>, <u>Zr</u>, Nb, <u>Ru</u>, Rh, <u>Pd</u>, <u>In</u>, Sn, Sb, <u>Ba</u>, <u>La</u>, <u>Ce</u>, Pr, <u>Nd</u>, <u>Sm</u>, <u>Eu</u>, <u>Gd</u>, <u>Tb</u>, <u>Dy</u>, <u>Ho</u>, <u>Er</u>, <u>Tm</u>, Yb, Lu, Hf, W, <u>Ir</u>, <u>Pt</u>, <u>Pb</u> and Bi</p>
Hybrid ALD/MLD^{III,IV,V,10,13-15}
<p><u>Li</u>, Al, Si, <u>Ca</u>, Ti, V, <u>Mn</u>, <u>Fe</u>, <u>Co</u>, <u>Cu</u>, Zn, Zr and <u>Eu</u></p>

phonons leading into higher efficiency¹⁶⁻¹⁹, as gas-barriers materials²⁰⁻²² or in metal-organic frameworks, where the inorganic central atoms are linked together by organic molecules in well-defined cage-like structures.^{III,V,13,23-25}

The ALD of oxide materials is a well-studied field, but the element choices for the hybrid ALD/MLD have notably less options, as seen in Table 1. The widely employed β -diketonate precursors (underlined in Table 1), where the cation is bonded from two ketone oxygen atoms, cover most of the studied elements, but unfortunately are non-reactive towards the most used MLD precursors, explaining the yet small number of developed hybrid processes.

The goal of the dissertation was to produce novel complex thin film oxide and hybrid materials through ALD and ALD/MLD technologies. The first two publications dive into the world of perovskite-type oxide cathode materials for solid oxide fuel cells, the ALD processes for the ternary $\text{SrCoO}_{3-\delta}$ ^I and quaternary $(\text{La,Sr})\text{CoO}_{3-\delta}$ ^{II} phases were, prior to this dissertation, missing from target parent $(\text{La,Sr})(\text{Co,Fe})\text{O}_{3-\delta}$ system. The hybrid ALD/MLD materials family prior this dissertation was limited in aluminium, titanium and zinc based, non- β -diketonate precursor derived amorphous hybrid materials. Since then, the hybrid ALD/MLD materials family has expanded rapidly to cobalt,^{IV} manganese,^{IV} copper,^{III} calcium,^V lithium,¹³ iron¹⁴ and europium¹⁵ hybrid materials after the realization of the highly reactive carboxylic acid precursors which work perfectly even with the low reactivity β -diketonate precursors.

2. Methodology

This chapter introduces the key characterization methods of the thesis work, namely X-ray reflectivity (XRR), grazing incidence X-ray diffraction (GIXRD), Fourier-transform infrared spectroscopy (FTIR), physisorption measurements and sample elongation studies. Other methods, such as X-ray fluorescence (XRF), induced coupled plasma optical emission spectrometry (ICP-OES), X-ray photoelectron spectroscopy (XPS) and atomic force microscopy (AFM) were applied as well, but are not reviewed here. XRF and ICP-OES were applied to study the medium-to-high molar mass elemental constitution of a whole sample, XPS to screen the elemental constitution, chemical surroundings and the oxidation state of some elements from the vicinity of a surface and AFM method in order to verify the roughness results derived from XRR measurements. The following brief summaries of the characterization techniques are far from complete and some other techniques might be equally able to provide the information gathered by the presented techniques.

2.1 X-ray reflectivity (XRR)

X-rays propagate approximately 10–200 μm inside a material, interacting with the electron density and crystal lattice of the material. Thus, it is advantageous to use X-rays for gathering information from thin films, assuming their thicknesses fall into the mentioned range. One particularly appealing method of analysing sample thickness, density and roughness is XRR. In this method, X-rays are directed to the sample from a low angle, usually of the order of 0.2° , and then the angle is increased while analysing the interference pattern is retrieved from the reflected beams.^{26,27} The sample density can be analysed from the critical angle (θ_c) seen in the low angle region where the X-rays no longer reflect from the surface, but begin to penetrate into the sample. The critical angle can be calculated using Equation (1), where λ stands for the X-ray wavelength, r_e classical electron radius and ρ_e electron density:²⁷

$$\theta_c = \sqrt{\lambda^2 r_e \rho_e \pi^{-1}} = k_1 \sqrt{\rho_e} \quad (1)$$

As noted in Equation (1), the critical angle is proportional to the square root of electron density of the material via constant k_1 . The density and refractive index of the thin film can be calculated with Equations (2) and (3), where ρ stands for density, A for average molar mass, N_A for Avogadro's constant, Z for average atomic number and n for refractive index:

$$\rho = \frac{\rho_e A}{N_A Z} = k_2 \rho_e \quad (2)$$

$$\sin \theta_c = \sqrt{(2 - 2n)} \quad (3)$$

The distance between the interference patterns, or the so-called Kiessig fringes, is used for calculating the sample thickness (d) shown in Equation (4), where m is an integer:²⁸

$$\sin \theta_{\text{maxima}} = m \frac{\lambda}{2d} \quad (4)$$

The surface and interface roughness profiles can be estimated from the decay rate of the intensity and the point of the incident angle where the Kiessig fringes are no longer visible. The root-mean-square (RMS) roughness (σ) is proportional to overall intensity by the equation (5):^{29,30}

$$I = I_0 e^{-k\sigma^2} \quad (5)$$

Typically, all of these film properties are calculated with computer programs designed for thin-film analysis, as was done in this thesis as well for each thickness, roughness and density value, where practically only the elemental ratio of the material is defined prior to the calculations. The previously presented XRR features are shown in Figure 1, where on the left side four example graphs are shown, followed by examples of critical angles with two different densities seen in (1), Kiessig fringes of thicker (top) and thinner (bottom) samples in (2) and samples with low, high and high roughnesses in (3) on top, middle and bottom, respectively.

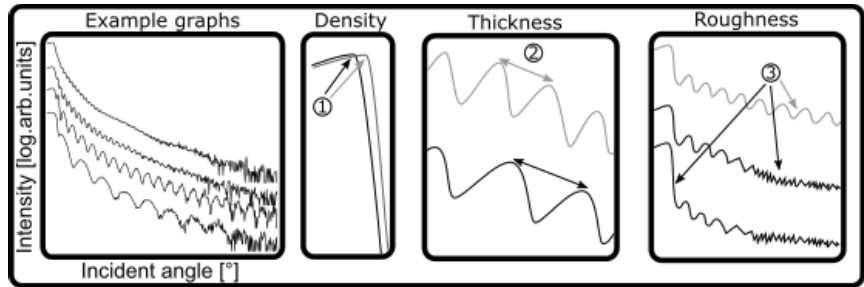


Figure 1. Four example XRR graphs are presented on the left, before the visualization of the important features of (1) critical angle, (2) Kiessig fringes and (3) the intensity or feature decay rates.

2.2 Grazing incidence X-ray diffraction (GIXRD)

X-ray diffraction (XRD) technique is a common method of analysing the structure of crystalline material and to identify the lattice stress in the sample, where the X-rays reflect from geometrical symmetry planes noted by Miller indices. In addition, X-rays might excite some atoms, which can be seen as an uneven baseline of the signal due to fluorescence. In a typical XRD measurement using Bragg-Brentano (θ - 2θ) configuration to detect the oriented crystal planes the angle of both the X-ray source and the detector are raised symmetrically while the sample is rotated. For normal bulk samples, this is a routine measurement procedure, but if applied for nanometer scale thin films, the resulting intensities from the sample can be inadequate due to the low measurement volume and here the signal from the substrate might be overwhelming. One way to approach thin film measurements is the surface-sensitive grazing incidence X-ray diffraction (GIXRD) technique, where the X-rays are projected constantly in a grazing angle slightly above (e.g. $+0.1$ – 0.5°) the critical angle θ_c and thus the measurement volume of the thin film is high enough to detect the signal. Even though the crystal phase is identifiable using powder diffraction databases, some peak intensities are typically low, different or slightly off-position. This is due to the fact that ALD films are made using a layer-by-layer technique where the resulting film might not be completely polycrystalline, and partly due to the stress/strain resulted from the lattice.^{31,32} GIXRD is useful for film stress analysis, as by measuring with varying grazing angles, a depth profile of residual stresses can be formed to study the effect of the substrate lattice (mis)match on the product's lattice parameters.^{31–33} If just a top few nanometers of the sample are in the scope of interest, a grazing incidence asymmetric Bragg (GIAB) geometry can be used where the grazing angle is below the critical angle at the “total reflection” area. In this configuration, the total reflection mode is dominating and merely a weak signal just from the surface can be seen.³⁴

In this dissertation, the GIXRD technique was applied for identifying the crystalline structures using Cu K_α X-rays. The main difference of the main diffraction methods, XRD and GIXRD, are compared in Figure 2. The graphs from the same thin film sample are measured with GIXRD (1) and XRD (3) methods in comparison to the silicon substrates, (2) and (4), respectively.

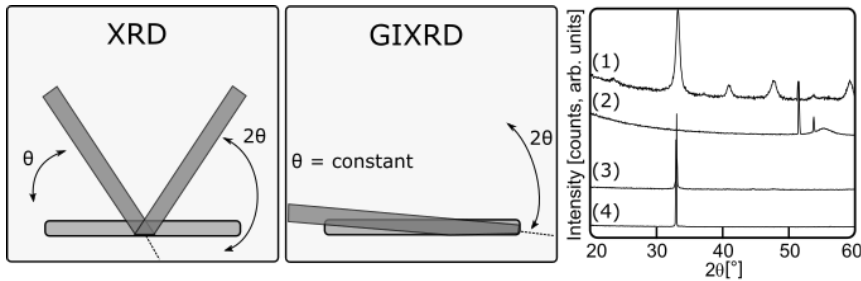


Figure 2. Left and middle: The main difference between Bragg-Brentano XRD technique and the GIXRD technique is the angle of the X-ray source. Right: Thin crystalline sample and the substrate was measured with (1,2) GIXRD and (3,4) XRD methods, respectively.

2.3 Fourier transform infrared (FTIR) spectroscopy

Infrared (IR) spectroscopy is a measurement technique based on IR radiation interacting with mainly the covalent bonds of molecules and crystalline structures, as the IR radiation passes through a sample and the absorbed wavelengths are measured.^{35,36} The signal point where a peak appears corresponds to the energy quantum required to activate a vibration mode in the sample molecule. The x-axis for IR spectrum is typically a wavenumber $\bar{\nu}$ [cm^{-1}], which is linearly dependant on the energy of the vibration mode, as seen from equations (6–8). The other symbols are the wavelength λ of the radiation describing the distance between the adjacent peaks of the wave, the frequency ν describing the number of the cycles per second of a wave, ΔE describing the energy required to excite the vibration mode from quantum ground state (E_0) to an excited state (E_1), c is the speed of light in vacuum and h is the Planck constant:

$$\bar{\nu} = \frac{1}{\lambda} = \nu * c \quad (6)$$

$$\Delta E = (E_1 - E_0) = h * \nu \quad (7)$$

$$\bar{\nu} = \Delta E * \frac{c}{h} \quad (8)$$

Fourier transform infrared (FTIR) instruments have advantages over older IR techniques such as high throughput (where the total source output can be passed through the sample continuously) and the speed advantage (where the spectra can be obtained in milliseconds due to rapid and accurate mirror movements), resulting in a high signal and an improved signal-to-noise ratio while the measurements are carried out in a fraction of a time. For a molecule vibration to be visible in IR spectrum, a changing electric dipole moment is required when any of the bonds are stretched or bent, i.e. the molecule must not be linear homodiatomic such as N_2 or O_2 .

The IR spectrum can be divided into three main regions; far-infrared ($<400 \text{ cm}^{-1}$), mid-infrared ($4000\text{--}400 \text{ cm}^{-1}$) and near-infrared ($13000\text{--}4000 \text{ cm}^{-1}$). Generally, near-infrared regions show only combinational peaks, where two or more vibration modes of the same or neighbouring parts of the molecule are combined. $4000\text{--}2000 \text{ cm}^{-1}$ region shows mainly the hydrogen-related (X–H) vibrations, while maybe the analytically most interesting carbon (C–X) and oxygen (O–X) related peaks are seen in the so-called *fingerprint area* of ca. $2000\text{--}650 \text{ cm}^{-1}$. The peaks from halogens, metals and crystal lattice vibrations are seen at lower wavenumbers ($400\text{--}100 \text{ cm}^{-1}$). Hydrogen bonding has a large impact in the analysis of FTIR spectrum, as it affects the bond strength of its counter-part and thus the resulting position of the peak in the spectrum. The hydration type of an inorganic compound can be estimated from the O–H stretching patterns seen at $3000\text{--}3800 \text{ cm}^{-1}$, where i.e. broad or sharp peaks indicate non-coordinated or coordinated species, respectively. Four example

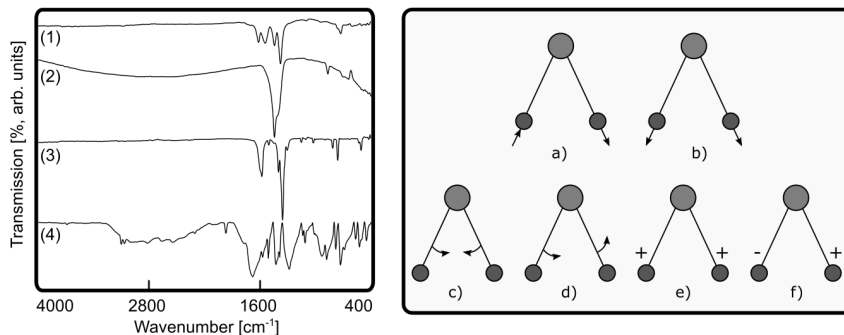


Figure 3. Four example spectra of (1) amorphous hybrid ALD/MLD film, (2) amorphous ternary oxide film, (3) crystalline hybrid ALD/MLD film and (4) terephthalic acid on a KBr are seen on the left. The three atom vibration modes of asymmetric and symmetric stretching, scissoring, rocking, wagging and twisting forms are seen in a-f, respectively.

spectra and the possible IR active vibration modes of three atom species are represented visually in Figure 3, which are a) asymmetric stretching, b) symmetric stretching, c) scissoring, d) rocking, e) wagging and f) twisting vibration forms. Some care should be taken when measuring the FTIR spectra, as subtracting the silicon spectrum from the sample+silicon spectrum, a substrate piece from the same silicon wafer is required. If even a substrate from the same wafer batch is subtracted instead, the baseline of the spectrum is heavily affected, as seen in Fig. 3 (left, 2). Samples (1) and (3) have correctly subtracted baselines and clear peaks are seen from C—O—Metal bonds near 1600 cm⁻¹, the major peak in (2) comes from carbonate group and the spectrum in (4) is the spectrum of terephthalic acid over KBr, precursor used e.g. in film (3).

2.4 Physisorption measurements

Physisorption is a shortened from physical adsorption, where a particle is adsorbed to the surface without forming a chemical bond, but is attached with van der Waals interaction.³⁶ The enthalpy difference of chemisorption to physisorption is roughly 10-folds higher with ca. -200 — -400 kJ mol⁻¹.

Brunauer, Emmett and Teller (BET) have developed a method which takes use of the physisorptive nature of certain gases to determine the surface area of materials.³⁷ Since the effective surface area of an adsorbed nitrogen molecule is known as ca. 0.162 nm² and the volume of the gas and the pressure can be measured precisely, the surface area which nitrogen molecules cover and thus the “BET surface area” of the sample can be estimated.³⁸ The pore volume can be similarly analysed by monitoring how much gas can be put into the measurement vial with the sample, while monitoring the pressure behaviour. The equation for BET theory (9) has V for adsorbed gas quantity, V_m as adsorbed monolayer gas quantity, p and p_0 as the equilibrium and saturation pressure and c as BET constant:

$$\frac{1}{V[(p_0/p)-1]} = \frac{c-1}{V_m c} \left(\frac{p}{p_0} \right) + \frac{1}{V_m c} \quad (9)$$

Using the BET equation by plotting the left-hand side of the equation $[V(p_0/p)-1]^{-1}$ on the y-axis and p/p_0 on the x-axis (see Fig. 4), a linear line should be established from the experimental results in p/p_0 range of ca. 0.05–0.35. Using the acquired plot, the slope and y-intercept can be applied to calculate the surface area covered by adsorbed molecules. However, some caution must be taken into account when accepting BET surface area results for highly porous materials or low mass samples.³⁸

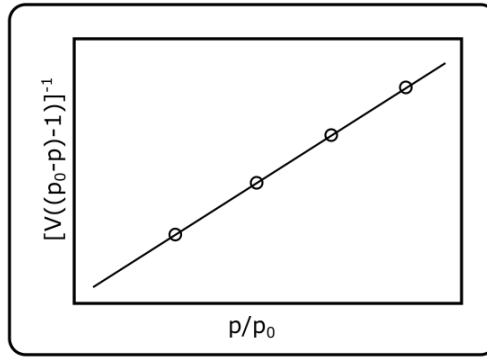


Figure 4. Example graph drawn from BET-equation to inspect the gas adsorption.

Pore volume analysis can be studied with e.g. Barrett-Joyner-Halenda³⁹ (BJH) method and nonlocal density functional theory (NLDFT). BJH is widely applied, but the newer NLDFT is more suitable micro- and mesoporous analysis for known pore types.^{38,40} Downsides of both methods include the BJH's underestimation of the pore sizes by ca. 25 % when the pore diameter is less than 10 nm, while for NLDFT the assumption of the pores being chemically homogenous, structureless and smooth.^{41,42}

In this thesis, moisture was evaporated for 24 hours at 150 °C in vacuum before BET analysis and for 48 hours at 150 °C before NLDFT pore volume analyses. The measurement takes place in 77 K, where the adsorption surface area of molecular nitrogen is known. The results expressed in this thesis are based on computer assisted calculations, where the user provides only the amount of material, calculated from its dimensions and density gathered from XRR measurements.

2.5 Elongation experiments

Studying of the mechanical properties such as elasticity, toughness and hardness for thin films includes controlled bending, stretching and scratching measurements. The elongation profile can be obtained when stretching the sample under a constantly increasing force, and features such as elastic region,

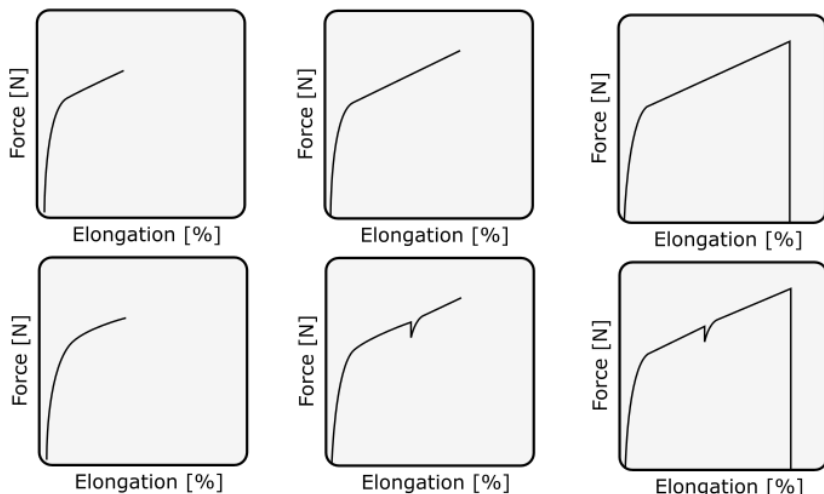


Figure 5. The top figures describe elongation profile of a single elastic material, while the bottom three figures show the breaking of the top layer as a small dent in the elongation profile. Leftmost figures show the formation from elastic to plastic region and rightmost figures show the breaking of the material.

plastic region and the breaking of the film can be analysed.⁴³ In the elastic region, the sample can be reverted back to its original stress-free state without structural damage, while in the plastic region, some irreversible damage is already happening. In Figure 5 top and bottom, the elongation profiles for an elastic film (=substrate) and for a case where thin film is seen to break before the substrate, are shown in top and bottom, respectively.

The elongation measurements were performed with a tensile tester, where the sample was first cut with a custom made razorblade jig into 2.25 mm wide strips, glued between abrasive papers from its long ends and then attached in to the tensile tester as shown in Figure 6. After careful adjustment of the sample, it was elongated with a constant rate of 0.5 mm/min and the required force was measured. The elongation studies require an elastic substrate, such as a polymer. A novel temperature resistant Kapton CS (DuPont) was chosen for these studies. The sample is then cut into smaller stripes determined by the tensile-stress tester's dimensions.

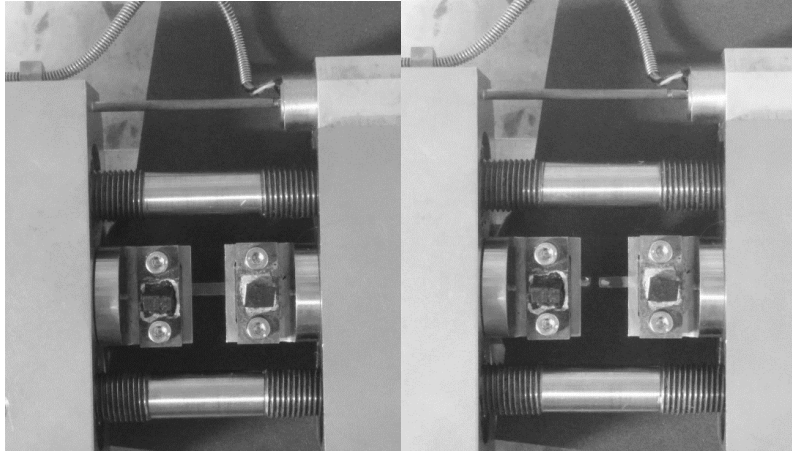


Figure 6. The tensile tester in a resting state (left) and when the sample is elongated until it's broken (right).

3. Thin film depositions of complex oxide and hybrid materials

This chapter goes through briefly the two main classes of vacuum deposition methods before presenting the key results of the dissertation work.

3.1 Physical and chemical vapour deposited thin films

Some of the fastest vacuum technologies to deposit thin films with a controllable cation ratio are physical vapour deposition (PVD) methods where the line-of-sight transport of material to substrate condenses into a solid, congruent film typically at 1–10 nm/s.⁴⁴ Even though the elemental controllability of the product is rather straightforward as the product generally has the same cation ratio as the source material,^{45,46} larger problems arise from shadowing effects induced from the line-of-sight -type deposition mode and the inevitable thickness variations which are poison to high aspect-ratio applications and in ultra thin film processes.⁷ The shadowing effects are welcomed to some applications such as in deposition of rod-type nanostructures for sensing or optical applications, or simply to create patterned films with a mask.^{47–49} One way to circumvent the shadowing issue is a deposition method where the product is yielded directly from a gaseous phase.

In a typical chemical vapour deposition (CVD) process, the chemical reactions occur on a hot surface where the precursors are introduced simultaneously and the product is grown all around at the same time, even in the cavities of the material.⁵⁰ The growth rate is affected mainly by the precursor arrival flux and/or surface kinetics. ALD is closely related to the CVD processes, but compared with typical CVD methods, the sequential introduction of the precursors in ALD enables better control over the film in high-technology solutions.^{5,51}

3.2 ALD of the binary oxides

The ALD is a unique method suited for fabricating (ultra) thin films on variously shaped and even on delicate substrates. The ideal growth is based on separate introduction of precursor gases until the desired film thickness is reached. The method is considered slow paced in comparison with other thin film production methods, which is understandable due to the sequentiality.

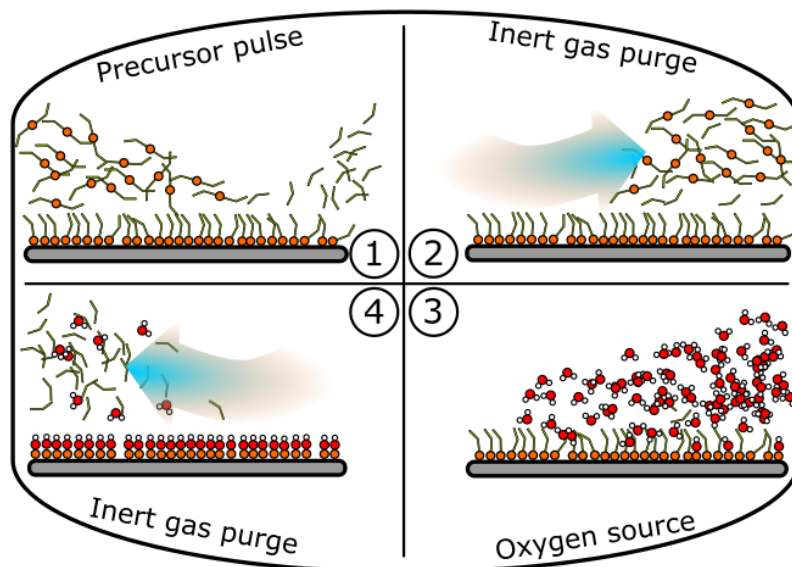


Figure 7. The schematics of an ALD cycle of a typical $ML_2 + H_2O$ process.

In Figure 7, the sequential pulsing of ALD precursors is presented for a typical $ML_2 + H_2O$ process: (1) The first precursor ML_2 is introduced to the surface || with -OH groups within an inert gas flow and the precursor molecules react with the reactive sites of the surface group forming ||-O-ML species and detaches a ligand HL. (2) The inert gas purge swipes the unreacted precursors away with the rest of the detached ligands and leaves behind a monolayer – or close-to-a-monolayer – of the chemisorbed precursor. (3) The second precursor pulse, H_2O , is let to react with the precursor layer forming the next layer of ||-O-M-OH, and the rest of the ligands are detached as HL species. (4) The inert gas purge empties the reaction chamber again and cleans the surface of the detached HL ligands and extra H_2O . The steps (1) – (4) form the so-called ALD cycle, which is repeated until the desired film thickness is reached.

If the strength of ALD comes from the sequential introduction of precursors, the strict sequentiality has its downsides as well. The time required to grow e.g. one micrometer thick film ($1/100^{\text{th}}$ of a cross-section of human hair) of colossally applied Al_2O_3 at e.g. 1.0 \AA/cycle , and let's say, 10 seconds of ALD cycle time would take more than a full day, which is one of the main reasons ALD is applied mainly for 1 – 100 nm films.^{5,52} Throughput can be defined as growth per unit time, which can be in terms of substrate wafers processed per hour or by deposited surface area per hour.⁷ An increase in the overall throughput value for single wafer ALD can be addressed by batch processes, where multiple wafers are deposited on simultaneously. However, larger surface areas and batch reactors require somewhat longer pulse and purge times to achieve full saturation, which nullifies some of the throughput advantages of the batch tools, and promotes the importance of heating, cooling, loading and unloading time it takes to change one sample vs. one batch of samples.

3.2.1 The optimization of the ALD cycle

The lengths for the precursor pulses and the inert gas purges need to be optimized to avoid either too long processes or uneven films. Typical time scales for one pulse or purge vary from 0.1 s to tens of seconds depending on the choice of reactor type, precursors and growth temperature. The growth behaviour can be analysed from the plot of pulse length vs. growth-per-cycle (GPC) as visualised for different scenarios in Figure 8. Monitoring the GPC in varying temperatures can reveal the optimal growth temperature range, often named as ALD-window where the GPC, or more importantly the product quality, is constant. In practice, there are always deviations from ideal ALD processes shown in Fig. 8(a,c), where GPC can continue to increase after a nominal saturation point, as seen in Fig. 8b, or the precursor might not chemisorb quickly or strongly enough with the surface groups, which is seen as abruptly declining thicknesses while the purge length is increased (Fig. 8d). Even the ALD-window is not usually completely flat, but it does not mean the repeatability would be lost or that the product quality would be insufficient, as visualised in Fig. 8(e).¹⁰ In a case where the ALD window is narrow and only a declining trend is seen as growth temperature is risen, it might indicate a diffusion of a precursor into the film at lower temperatures providing more reactive sites and at higher temperatures the diffusion out of the film gets stronger.⁵³ However, the diffusion phenomenon is more typical for ALD/MLD processes and rare for ALD processes. In addition, the combined effect of increased reaction activation rate and the decrease of reactive sites might change the shape of the ALD window curve.⁵⁴ Moreover, even though the temperature-to-GPC analysis gives some important information regarding the growth process, maybe GPC should not be focused as much as it has historically been, but the product quality such as resistivity, surface roughness, chemical composition or density.

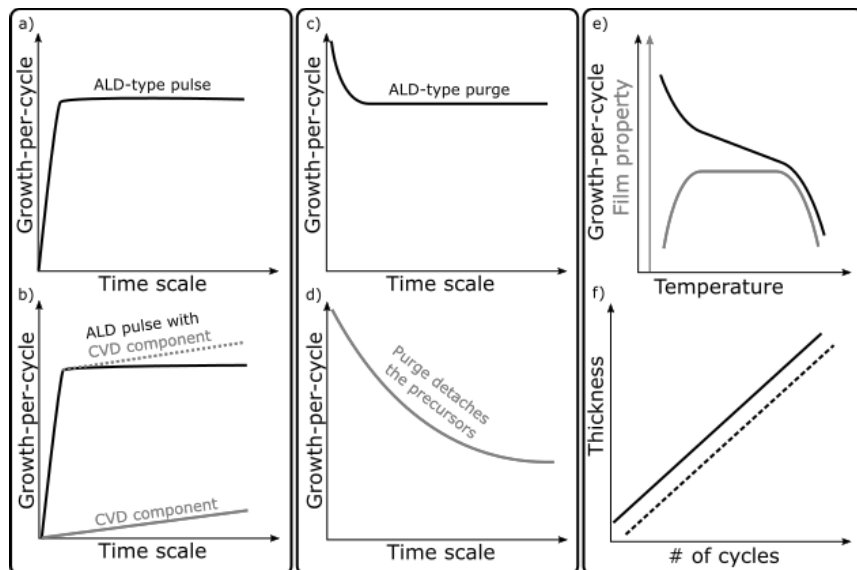


Figure 8. Typical ALD characteristics are visualised where the saturation of the ALD pulse and purge are shown in (a) and (c), inclusion of a CVD-type growth component in the ALD-pulse is shown in (b) and low sorption of the precursor is seen as declining GPC in (d), ALD-window in (e) and the linear increase of the thickness with ALD-cycles is shown in (f).

In the optimized ALD growth process, a linear increase in the repetitions of the ALD cycles would mean perfectly linear increase in film thickness (Fig. 8f). Even though the growth linearity is achieved in the higher number of deposition cycles, the initial GPC during the first few layers of the process might exhibit increased or decreased values. The surface of the substrate might either promote or inhibit the growth of the film in comparison to the precursor oxide layer due to e.g. different amounts of reactive sites or by different growth modes of the chemically different surfaces, discussed also in ternary film growth section near Fig. 11.^{54,55} The deposition process at the first few layers is seldom discussed in ALD studies, but recognizing this and studying the results with e.g. microscopic or QCM methods might provide valuable information of the growth process when the fabrication goal is in an ultra-thin film, as often required for applications.^{5,13,56}

3.2.2 Precursors

A typical precursor molecule consists of an inorganic atom surrounded by one or more ligand groups. The key requirements for the ALD precursors are (1) sufficient volatility, (2) resistance to thermal decomposition at the growth temperature, (3) affinity for detaching one of its ligands to create a stronger chemical bond with the surface group, (4) self-limiting growth, (5) fast reaction rate with the surface and (6) gaseous reaction by-products which don't react with nor readsorb to the surface.^{6,54} The list of preferred requirements is even longer, and thus some compromises are always required. The precursors

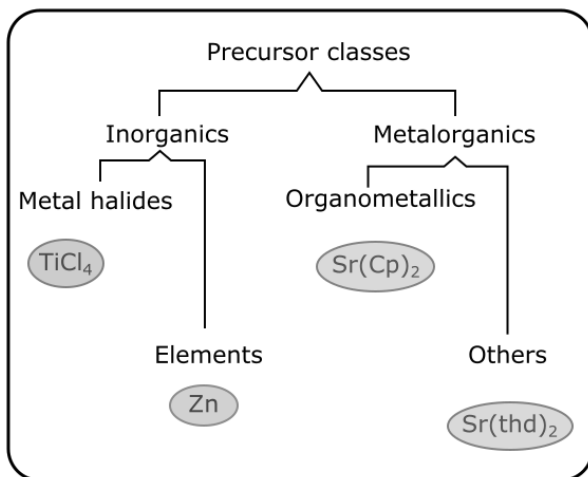


Figure 9. The ALD precursor-tree.

can be classified with two main groups – inorganics and metalorganics, seen in Figure 9.

The inorganics consist of metal halides and pure elements of which neither are experiencing steric hindrance induced by the bulky ligands. Halides are generally applied due to their high reactivity, small ligand size and good thermal stability. Major downsides include the gaseous by-products combined with hydrogen-containing precursors yielding halic acids, which can etch the film surface or readsorb to the surface as unwanted impurities which fortunately are diminutive when the growth temperature is raised.⁵⁴⁻⁵⁷⁻⁵⁹ Examples of pure elemental precursors include Mg, Cd, Mn, Zn, Ga, In, Sn (c.f. Ref ⁵⁴), which have advantages on the nonexistent impurities and steric hindrance, but might endure problems in CVD-type growth behaviour and low vapour pressures. The second main group, metalorganics, can be further divided into two subgroups – organometallics and others. Organometallics are precursors with metal–carbon –bonds such as alkyls and cyclopentadienyls, and the others consists e.g. of alkoxides, β -diketonates, amides and amidinates.⁵⁴ Organometallics generally react quite readily with hydroxyl groups, meaning they can be employed with “gentle” oxidizer H_2O , but on the other hand, stable alkyls are not available for many metals, and the deposition temperatures can be limited due to their self-decomposition.⁶ If the precursor is not reactive towards water, for example more reactive ozone is a valid choice. Ozone, mainly used for e.g. β -diketonate precursors, is such a strong reactant that it oxidizes even the surface layers of the underlying substrate, and as it is not a stable form, the concentration of the ozone may vary on different regimes of the reactor chamber. Ozone burns the organic part of the film away, usually leaving a residue of carbonates inside the film which also are practically non-existent when the deposition temperature is raised.⁶⁰⁻⁶⁴ In general at higher temperatures, the amount of impurities is lower but not all substrate materials can endure temperatures of 300+ °C, which may cause difficulties on the precursor selection.

3.3 ALD of the complex oxides

The ALD of ternary and quaternary oxides, that is oxide materials with two or three metal species, respectively, is similar to ALD of binary oxides with mixing of the binary deposition cycles to reach the desirable composition. However, some distinct extra features dominate the deposition of the complex oxides which are the cation stoichiometry control, growth-per-supercycle and growth surface deviations.

This chapter discusses the growth of complex oxides. For distinctness in describing the complex systems, a notation of *A* and *B* in *cursive* are applied for precursor cycles for materials A and B, respectively, including the purges and oxidative pulse in the ternary system.

3.3.1 Ternary and quaternary oxides

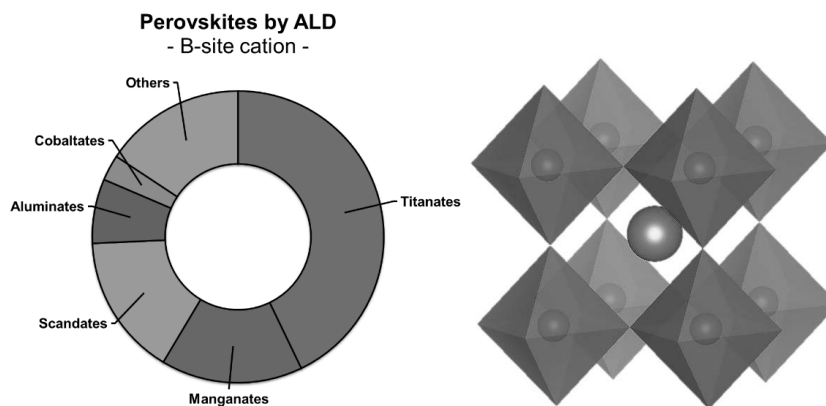


Figure 10. Proportions of studied perovskite-type ($ABO_{3-\delta}$) materials (left) and the illustration of the perovskite crystal structure where a large central atom A is surrounded by cornersharing BO_6 octahedrons.

Perovskite-type ($ABO_{3-\delta}$) materials have been in the major focus of the complex oxides by ca. 80-90 % share. Perovskite-type materials have been studied using ALD since 1997 when Seim et al. published the processes for two materials; $LaCoO_{3-\delta}$ ⁶⁵ and $LaNiO_{3-\delta}$.⁶⁶ The 2nd most studied materials group of spinels, with $AB_2O_{4-\delta}$ stoichiometry, have been researched since 1993 when Huang et al. published a robust method for producing $MgAl_2O_4$ at high temperatures.⁶⁷ The rest of the materials type can be counted single-handedly, which include misfit-material $[Ca_2CoO_3]_{0.62}[CoO_2]$ ⁶⁸ fabricated from $Ca(thd)_2$ and $Co(thd)_2$ precursors, and $SrTa_2O_6$ from bication precursor.⁶⁹ Since the 90's, without considering the doping of binary films, over a hundred ternary and quaternary processes have been published, where roughly one fifth of them have been considering high- κ material $SrTiO_3$ (STO), and the majority of the precursors have been either β -diketonates or iso-propoxides (mainly

STO's).^{6,8} Figure 10 visualises the perovskite-type ternary oxide processes arranged by their B-site cation and the crystallographic structure of a perovskite. Practically all the quaternary oxides have been solid oxide fuel cell (SOFC) materials while some are studies on multication precursors.^{70–74,11}

3.3.2 The growth optimisation

The deposition of ternary and quaternary ALD films is more difficult than binary films due to the requirement of a certain cation stoichiometry of the final product. The overlap of ALD windows from separate binary oxide processes is not necessarily wide, although it is debatable how large concern this is as the binary ALD window studies are conducted over different substrate material and typically with different metrics than with ternary films. Typically, the ternary ALD window is determined by studying 1:1 pulsing ratio of *A* and *B* cycles, and when the suitable temperature is found, the cation stoichiometry is optimized by the so-called supercycle analysis, where the pulsing ratios for *A* and *B* are varied as presented in Equation 10:

$$N \times (a \times A \rightarrow b \times B) \quad (10)$$

where *N* is the total repetition of the supercycles, *a* is the repetition of *A* cycles and *b* repetitions for *B*. The resulting cation ratio from 2:1 pulsing ratios of *A* and *B* usually does not usually equal to 2:1 molar ratio of the product due to different physical size of the precursors and the growth surfaces of the first and the second cycle of *A*. As presented in Figure 11, the deposition of *A*₁-*B*-*A*₂-*A*₃ has different growth surfaces for each of the three *A*-precursor cycles, yielding varying amounts of deposited material with each step. In addition, one ALD cycle rarely forms a complete monolayer,⁷⁵ which provides a unique growth surface to *A*₃ as the material *B* is partially visible under *A*₂. Moreover, the effect of the one deposited layer might affect the growth of even the next few layers, as demonstrated clearly by e.g. Elam and George with QCM studies on ZnO/Al₂O₃ laminates.⁷⁶

Demonstrations of good composition control for ternary oxides has been published e.g. by Vehkamäki et al. and Kosola et al. with the early studies of SrTiO₃.^{60,77} and by Elliott and Nilsen on five ternary compounds.⁷⁸ The profound growth mechanism studies from two combined binary processes by Elliott and Nilsen yielded well correlated fit profiles derived from two theoretical

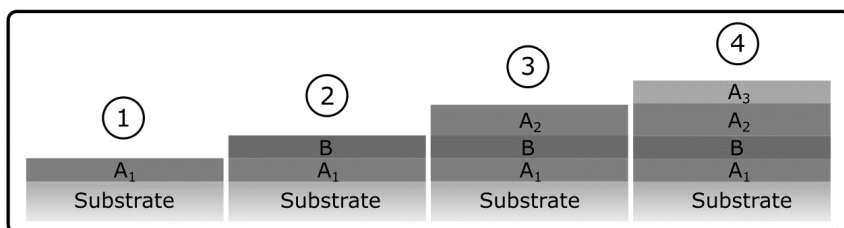


Figure 11. Different growth surfaces are demonstrated for the same *A*-precursor.

models. In the first model, combustion only (CO-model), the ligands stay intact on the cation, detached only after ozone pulse is introduced. The second model is combustion and partial brønsted elimination (CAPBE-model), where the main idea is a combustion-related forming of hydroxyl groups assisting in the growth by aiding to detach one ligand before the ozone is introduced. These models are based on early work e.g. Ritala et al.,^{79,80} Ylilammi⁸¹ and Lie et al.,⁷³ where the growth rates of different precursors were found to be inversely related to the area they occupy on the surface.

In publications **I** and **II**, assumed that one of the ligands is detached from the precursor as the precursor reacts with the surface groups as in the CAPBE method, a correlation to the molar mass of the remaining ligands is noted. It was observed with chemically similar ligands acetyl acetate (acac) and 2,2,6,6-tetramethyl-3,5-heptanedione (thd), see Fig. 12, that the physical size affects the growth rate due to steric hindrance and in addition, cross-sectional surface area of the ligands is related to the molar mass, since they are constituted from similar elements. This gives a handy tool to quickly estimate the surface areas or steric hindrances of the precursors, although for more accurate calculations, parameters such as packing geometry and three-dimensionality must be taken into account as the ligand shapes are not perfectly circular or flat.

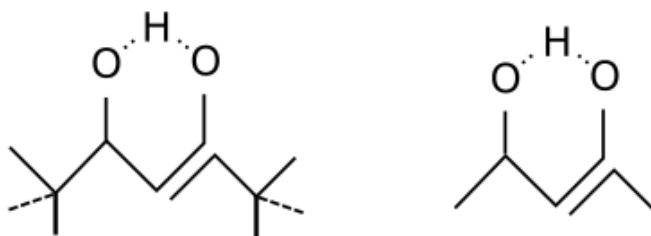


Figure 12. Simple models for the larger thd (left) and the smaller acac (right) ligands.

The idea of the molar mass correlating with the surface area can be visualized by plotting the cross-sectional surface areas of various literature reported hydrocarbons and some commonly employed gaseous substances against their molar masses, shown in Figure 13.^{82,83} It is seen that a correlation exists, although not being completely linear since at higher molar masses (dyes) the formation of clearly 3D structured molecules affect the adsorbed surface area.

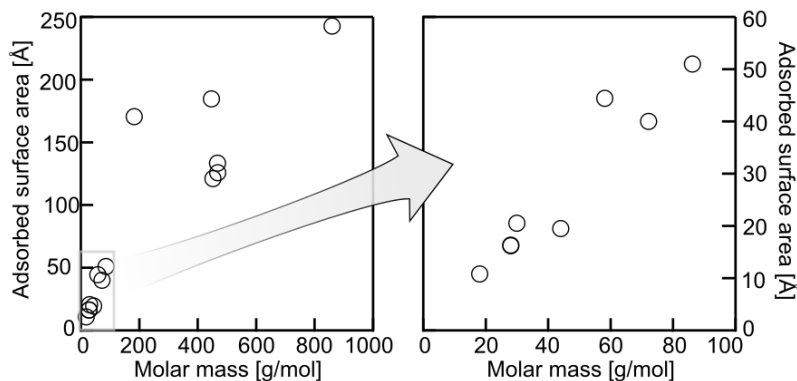


Figure 13. Correlation of molar mass vs. cross-section surface area in wide and narrow ranges.

3.3.3 Solid oxide fuel cell cathode materials

In the first part of the dissertation, ALD processes for complex ternary^I and quaternary^{II} oxide materials related to intermediate temperature solid oxide fuel cell (IT-SOFC) cathode materials were developed. The objective is to work at intermediate temperatures, but the optimal operating temperature can be debated as not only the lower temperature promotes a longer lifetime, shorter start-up times and wider application base, it also reduces the Carnot efficiency, risks the material for carbonate poisoning and decreases the reaction kinetics.⁸⁴ The middle ground for SOFC operation is somewhere at 500–600 °C, where Gadolinium-doped ceria $\text{Ce}_{0.9}\text{Gd}_{0.1}\text{O}_{1.95}$ is one of the best choices for electrolyte material for its high ionic conductivity,⁸⁵ and i.e. copper or nickel ceria mixtures can act as a high-performance anode material.⁸⁶ Cathodes have to excel in the reduction of molecular oxygen, transport of the oxide ion to the electrolyte and participate in distribution of the electric current.⁸⁴ In the intermediate temperatures, the polarisation losses of the cell are high due to slow kinetics in oxygen reduction and oxide transportation.⁸⁷ One of the most studied cathode materials, $(\text{La},\text{Sr})\text{MnO}_{3-\delta}$, is not active enough at intermediate temperatures, but the $(\text{La},\text{Sr})\text{CoO}_{3-\delta}$ has been identified as perhaps the most promising candidate, which has a large drawback from the high thermal expansion coefficient (TEC) resulting in incompatibility with most of the applicable electrolytes.^{84,86} La-for-Sr substitution in the A-site affects the electrical conductivity of the material, while the TEC can be tuned down even to nearly match with the $\text{Ce}_{0.9}\text{Gd}_{0.1}\text{O}_{1.95}$ by substituting iron for cobalt in the B-site. To further improve the mixed ionic-electronic conductor (MIEC) properties in thin film cathodes, Prestat *et al.* demonstrated 1–1.5 orders of magnitude reduction to polarization resistance at 500°C by eliminating the bulk diffusion pathway with the reduction of the film thickness of the $(\text{La},\text{Sr})(\text{Co},\text{Fe})\text{O}_{3-\delta}$ cathode from 766 nm to just 16 nm.⁸⁸ Other studies state that in bulk materials, the oxygen reduction reaction (ORR) is the rate-limiting step, which can be confronted by adding more reactive sites by increasing the surface area or by increasing the amount of triple points where cathode, electrolyte and oxygen meet.^{89–92} In conclusion, a high-surface-area thin-film material would be the

best solution for high-performance cathode, and one of the best IT-SOFC cathodes is (La,Sr)(Co,Fe)O_{3-δ}.^{93,94} Prior to this thesis, the family of ternary and quaternary ALD processes to cover the (La,Sr)(Co,Fe)O_{3-δ} elements were missing SrCoO_{3-δ} and (La,Sr)CoO_{3-δ} constituents.^{64,65,73,95}

3.3.4 Case studies: SrCoO_{3-δ} and (La,Sr)CoO_{3-δ}

For the SrCoO_{3-δ} ALD process, the optimal growth temperature was found in between 290–330 °C, where below the growth window some thickness patterns were observed, and above the window the precursors began to thermally decompose. Similar effects were seen for the (La,Sr)CoO_{3-δ} process, except with the ALD-window temperature range of ca. 250–310 °C. The final deposition temperatures for the two materials were 310 and 290 °C, respectively.

The precursors for the studies were chosen from the β-diketonate family due to the excellent performance with O₃ and due to their easy preparation and handling, as they can be synthesised within 2 days and they are not typically very sensitive to air or moisture.⁹⁶ The optimal precursor temperatures for the SrCoO_{3-δ} process were found to be 200 °C and 135 °C for Sr(thd)₂ and Co(acac)₃ respectively, while in (La,Sr)CoO_{3-δ} process, the precursor temperatures for La(thd)₃, Sr(thd)₂ and Co(acac)₃ were 175, 200 and 142 °C, respectively. The optimal temperature was determined with ca. 100-200 mg of precursor consumption during the deposition of ca. 100 nm film.

The pulse and purge characteristics were first optimized separately for the binary processes before mixing for ternary (SrCoO_{3-δ})^I or quaternary ((La,Sr)CoO_{3-δ})^{II} processes, seen in Figure 14, where Sr(thd)₂ has the highest, Co(acac)₃ second highest and La(thd)₃ has the lowest GPC. The GPC values are in line with the scheme where the remaining precursor + ligand(s) has a certain surface area blocking the neighbouring surface sites. The surface areas taken by the physisorbed or chemisorbed precursors are from smallest to largest; Sr(thd)₂ < Co(acac)₃ < La(thd)₃. In the final products, the pulsing lengths (with N₂ purges in parentheses) for SrCoO_{3-δ} studies were optimized to Sr(thd)₂ 1.5 s (2.0 s) → O₃ 3.0 s (2.5 s) → Co(acac)₃ 1.5 s (1.5 s) → O₃ 3.0 s (2.5 s). For the (La,Sr)CoO_{3-δ} studies, the metal precursor pulses were lengthened to 2.0 s with 1.5 s purge, while the O₃ pulses and purges were kept the same.

The supercycle studies were then conducted to investigate the cation control of the deposition processes. The goal for the SrCoO_{3-δ} process was to obtain the 1:1 cation ratio measured with the XRF method, which was fortunately obtained immediately with the 1:1 pulsing ratio of the precursors at the chosen deposition temperature. For the (La,Sr)CoO_{3-δ} process, the optimization process was somewhat more laborious as the optimal cation ratios were optimized in respect with the two A-site cations and with the A-to-B site cations com-

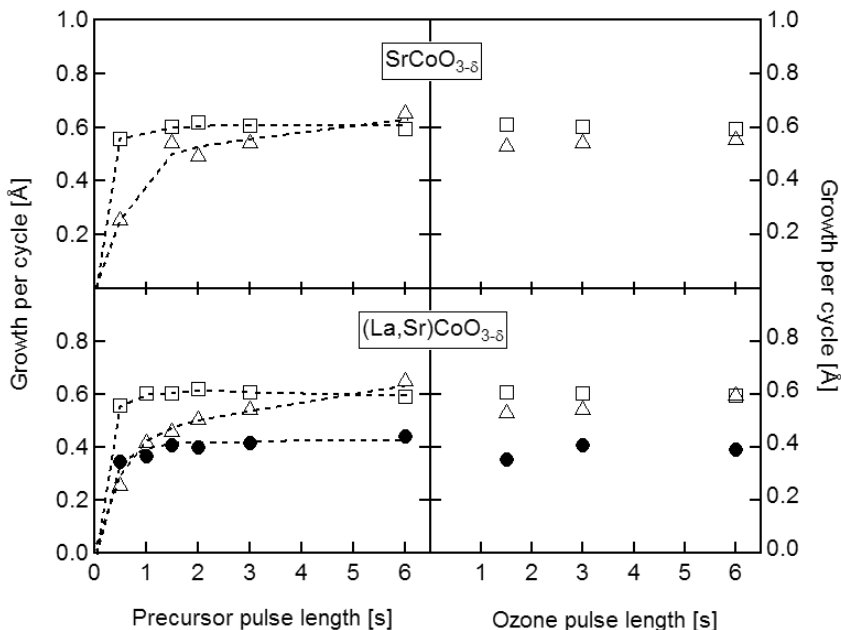


Figure 14. Growth characteristics for $\text{SrCoO}_{3-\delta}$ (top frames) and $(\text{La,Sr})\text{CoO}_{3-\delta}$ (bottom frames), for metal precursors (left frames) and ozone pulsing to each precursor (right frames). $\text{La}(\text{thd})_3$ is denoted as \bullet , $\text{Sr}(\text{thd})_2$ as \square and $\text{Co}(\text{acac})_3$ as \triangle .

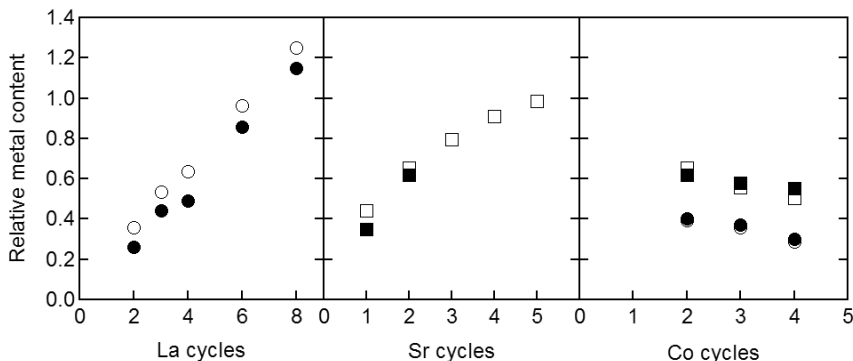


Figure 15. Relative amounts of A-site cations lanthanum (\circ and \bullet) and strontium (\square and \blacksquare) compared to B-site cation cobalt measured with XRF (open symbols) and ICP-OES (closed symbols) methods.

bined to obtain the optimal $(\text{La}_{1-x}\text{Sr}_x)\text{CoO}_{3-\delta}$ ($x = 0.3-0.7$) structure, where the material exhibits metallic conductivity and the structure should crystallize into the rhombohedral or cubic phase.⁹⁷⁻⁹⁹ The cation ratios were also studied with the inductive coupled plasma optical emission spectrometry (ICP-OES) method in addition to the non-destructive XRF method, shown in Figure 15. The deposition scheme for $\text{La}(\text{thd})_3$ supercycle studies had the amount of $\text{Sr}(\text{thd})_2$ and $\text{Co}(\text{acac})_3$ cycles kept constant (1 and 2, respectively) and only the number of $\text{La}(\text{thd})_3$ cycles were increased. The precursor cycles were mixed as much as possible within the supercycle to aid the crystallization of the amorphous

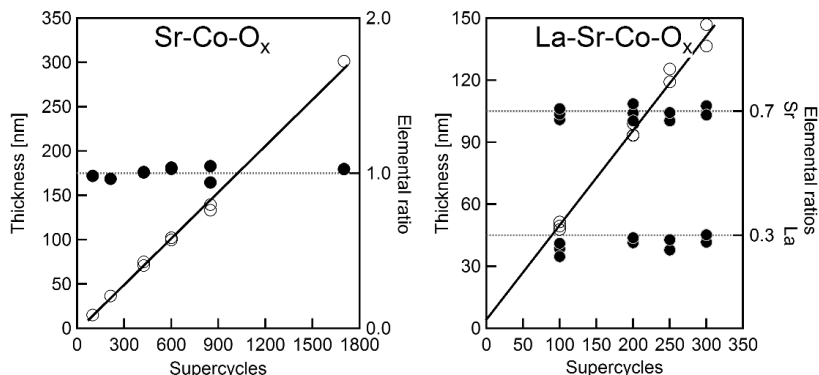


Figure 16. Growth linearity studies with the target amorphous compositions, where the hollow spheres denote thickness vs. supercycles and black spheres to cation composition. The dashed lines describe the target molar values scaled to cobalt proposition of 1.0.

product in the later phase. For $\text{Sr}(\text{thd})_2$ supercycle studies, the number of $\text{La}(\text{thd})_3$ and $\text{Co}(\text{acac})_3$ cycles were kept constant at 3 and 2 cycles, and for the $\text{Co}(\text{acac})_3$ supercycle studies, the number of $\text{La}(\text{thd})_3$ and $\text{Sr}(\text{thd})_2$ cycles were kept as 3 and 2, respectively. It was found out that the portion of lanthanum in the product was linearly dependent of the number of cycles, while for $\text{Sr}(\text{thd})_2$ it was non-linear. This indicates $\text{Sr}(\text{thd})_2$ having slightly lower GPC when deposited over Sr-rich surfaces than La-rich surfaces, while for $\text{La}(\text{thd})_3$ the surface reactions occur equally. For the later studies, two products were chosen which had $0.3\text{La}-0.7\text{Sr}-1.0\text{Co}$ and $0.7\text{La}-0.3\text{Sr}-1.0\text{Co}$ cation ratios.

The growth linearities for both $1.0\text{Sr}-1.0\text{Co}-\text{O}_x$ and $0.3\text{La}-0.7\text{Sr}-1.0\text{Co}-\text{O}_x$ were then studied. It was found that the target metal compositions were hold within $0.47-0.52$ for Sr in $\text{SrCoO}_{3-\delta}$, and $0.23-0.30$ for La and $0.67-0.72$ for Sr in $(\text{La},\text{Sr})\text{CoO}_{3-\delta}$ in each deposition, in addition to good linearities from multiple of duplicate measurements, shown in Figure 16. The trendlines to describe the linearity had R^2 values of 0.995 and 0.990 , respectively, and they cross the y-axis at -4.4 nm ($+2.8$ nm when the 1700 cycle point is removed) and $+2.8$ nm, for $\text{SrCoO}_{3-\delta}$ and $(\text{La},\text{Sr})\text{CoO}_{3-\delta}$ respectively. This indicates that the substrate is somewhat aiding in the growth of the first few layers, and that the growth is then stabilized quickly.

The as-deposited films had some carbonate impurities seen at $\text{ca. } 1440\text{ cm}^{-1}$ when studied with the FTIR method, shown in Figure 17 for $1.0\text{Sr}-1.0\text{Co}-\text{O}_x$ on top and for $0.3\text{La}-0.7\text{Sr}-1.0\text{Co}-\text{O}_x$ at bottom. The carbonates are typical impurities in some ozone processes, especially in strontium films, where SrCO_3 forms easily.⁷³ The carbonate groups detach when the film is heated to 700°C and above, which is typically a temperature area where the atoms begin to rearrange in the lattice.¹⁰⁰

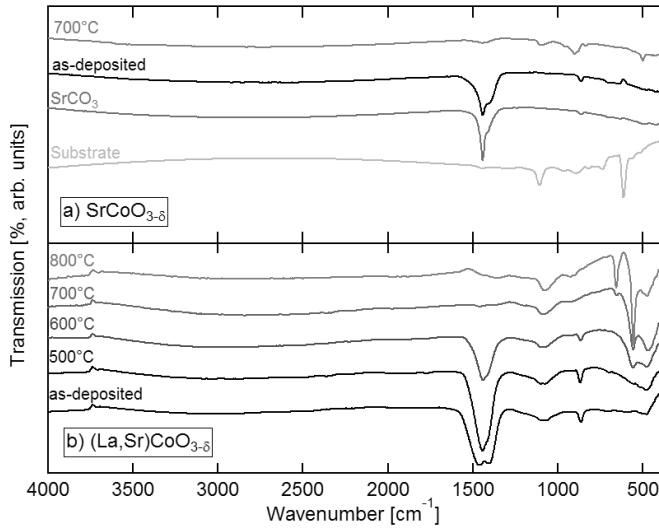


Figure 17. FTIR spectra relevant to a) $\text{SrCoO}_{3-\delta}$ and b) $(\text{La,Sr})\text{CoO}_{3-\delta}$ depositions. The denoted temperatures indicate the post-deposition annealing temperature under O_2 gas flow, revealing the leaving of the carbonate impurity.

The detachment of the carbonate groups at the high temperatures might indicate of forming of other, most likely crystalline structure. This idea was studied with the GIXRD method after annealing the films in different atmospheres under N_2 , O_2 or airgas flows. For the stoichiometric Sr-Co-O_x , the samples were heated from 550 °C up to 850 °C in two different atmospheres (N_2 and O_2) to study the formation conditions of the crystalline structure, seen in Figure 18a. It is seen that while 550°C was not enough for structural changes, 600 °C is sufficient for the formation of rhombohedral (R32) low-temperature phase of $\text{SrCoO}_{3-\delta}$, namely $\text{Sr}_6\text{Co}_5\text{O}_{15}$ (PDF Ref. 00-049-0692) with unit cell parameters of ca. $a = 9.4890 \text{ \AA}$, $b = 9.4890 \text{ \AA}$ and $c = 12.3650 \text{ \AA}$.^{101–103} At 850°C in both atmospheres, the structure is decomposed back into the binary oxides. The peaks are slightly shifted to lower angles when annealed in O_2 atmosphere, indicating slightly larger unit cell. Similar approach was applied to $0.3\text{La}-0.7\text{Sr}-1.0\text{Co}-\text{O}_x$ as well under more SOFC related O_2 and air-gas (mixture of 80% N_2 and 20% O_2) atmospheres, where the correct phase is seen to form at 600 °C and to decompose at 900 °C. There were no differences in GIXRD patterns between the choice of atmospheres, thus only one GIXRD from each temperature is shown for clarity in Figure 18b. The $(\text{La}_{0.3}\text{Sr}_{0.7})\text{CoO}_{3-\delta}$ forms, according to van Doorn et al.,¹⁰⁴ near perfect cubic structure (Pm3m) with unit cell parameters of ca. $a = b = c = 3.8323 \text{ \AA}$, while the $(\text{La}_{0.7}\text{Sr}_{0.3})\text{CoO}_{3-\delta}$ forms a rhombohedral phase (R-3c) with unit cell parameters of ca. $a = 5.4481 \text{ \AA}$, $b = 5.4481 \text{ \AA}$, $c = 13.2277 \text{ \AA}$. This is most likely the situation here as well, since according to the powder diffraction file database for the structures (cubic: 00-048-0137, rhombohedral: 04-013-1001) the XRD patterns are similar except in peaks at 2θ values of 23.2–23.5° and 47.4–48.1° where the rhombohedral has somewhat stronger peak intensities.

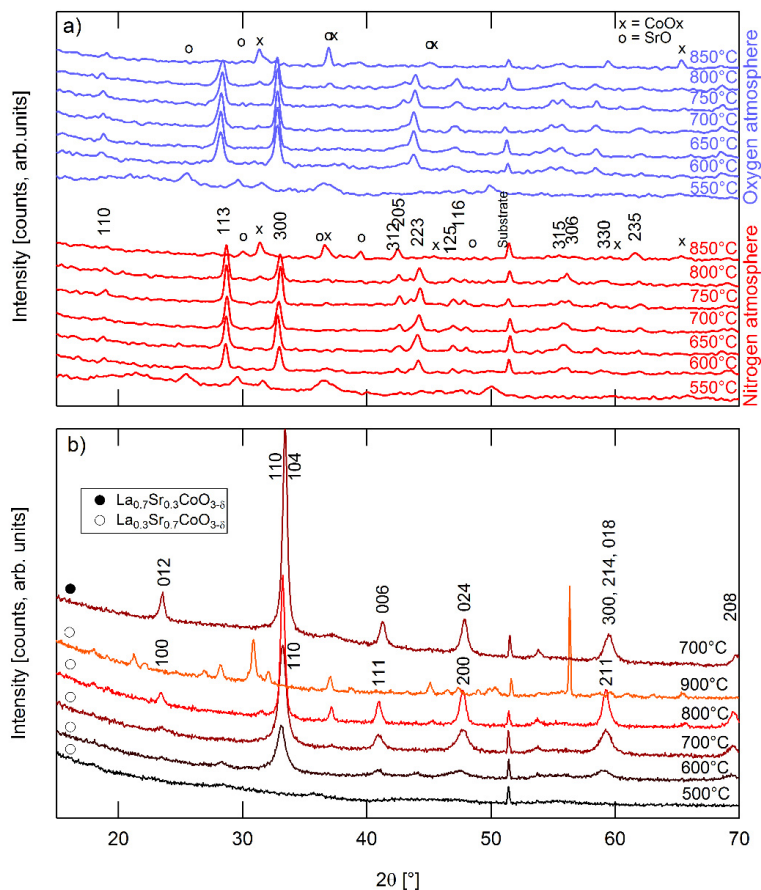


Figure 18. The GIXRD studies of the post-annealed thin films of a) $\text{SrCoO}_{3-\delta}$ and b) $(\text{La,Sr})\text{CoO}_{3-\delta}$ reveals crystalline structures.

3.4 Hybrid atomic/molecular layer deposition

The molecular layer deposition (MLD) method, invented in the early 90's by Yoshimura et al.,^{10,105,106} describes the deposition of organic molecule layers similarly as inorganic compounds are deposited with ALD. MLD precursors, such as halides, isocyanatos or isothiocyanatos, react with e.g amine or diol to form a combination of dimolecular film, and materials such as polyethylene terephthalate (PET) and Kevlar can be fabricated.^{10,107,108} Pure MLD films have three key properties listed in recent Yoshimura's review,¹⁰⁹ which are ultra-thin conformal organic films, tailored organic films and selective organic films, applicable e.g. in diffusion barriers, wavelength sensitized solar cells and in area-selective deposition masks, respectively.

The ALD and MLD techniques can be combined to create a hybrid material which has properties from both inorganic and organic worlds. In hybrid ALD/MLD the inorganic and molecular precursor cycles are mixed to yield

either hybrid inorganic-organic structures, superlattice structures or nanolaminates depending on the cycle proportions. While the definitions are not completely unambiguous, generally in hybrid films inorganic and organic layers are alternated, in superlattice structures typically the thin organic layers are separated with thicker inorganic layers and in nanolaminates, all the layer thicknesses are thicker, measured in several nanometers.¹⁰ The repeating superlattice structure has exciting phonon dispersion properties applicable in for example thermoelectrics, where the power factor can be significantly enhanced by intelligent materials design.^{16,18,110,111} Just in recent years, ALD and ALD/MLD methods have been utilised to form crystalline metal-organic framework (MOF) structures either after post-deposition vapour exposure,²³ post-deposition processing^{24,25} or as a fast one-step deposition methods.^{III,V,13} Thin film MOFs can be applied¹¹² e.g. in solid state batteries,¹³ catalysis,¹¹³ drug-delivery,¹¹⁴ chromatographic sieves¹¹⁵ and ultra-sensitive sensors.¹¹⁶ The commonly yielding amorphous hybrid thin films are useful e.g. in phosphors¹⁵, solid state battery electrodes¹¹⁷ and protective coatings^{22,118}, and more applications should arise as the shroud of novelty is no longer affecting.

Typical hybrid ALD/MLD organic precursor is a diol, such as hydroquinone (HQ), and not too many other options have been studied prior the beginning of this dissertation work.¹⁰ Other possible functional groups include amines, carboxylic acids and the heterobifunctional mixtures, such as 4-aminophenol (4-AP). Carboxylic acids differ majorly from diols and amines by the possibility to form highly stable, resonance-stabilized complexes and with multiple different coordination options depending on the metal constituent.¹¹⁹ The research on ALD/MLD of carboxylic acids has roots in 2008 when the group in Oslo¹²⁰ studied unsaturated¹²¹ and saturated linear¹²² and saturated aromatic¹²³ organics with combination of trimethylaluminium (TMA). Those studies yielded smooth amorphous films with decently high growth rates of ca. 5–10 Å/cycle. The carboxylic acid group reacts completely with the inorganic species, seen

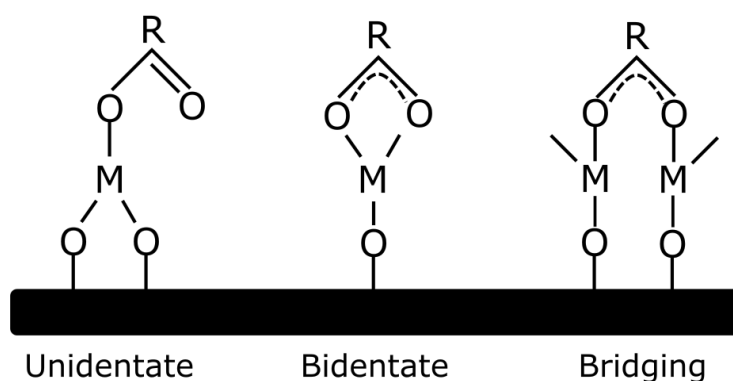


Figure 19. The carboxylate group coordination to metal(III).

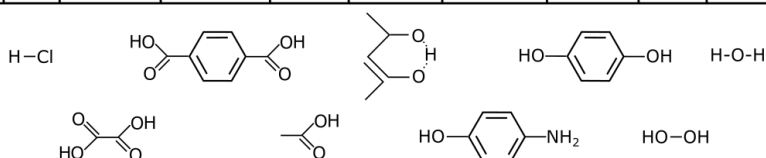
from the FTIR spectrum as the disappearance of the R-COOH –bands. Moreover, it can form either unidentate, bidentate or bridging structures, visualized in Figure 19.¹¹⁹

During the dissertation studies, the typical precursors hydroquinone (HQ) and 4-aminophenol (4-AP) were found not to possess the ability to react with β -diketonate precursors. Thus a more reactive but simple precursor was sought to replace the organic species and the carboxylic acids were studied among the systematic research. The carboxylic acid group was found to react surprisingly well with the β -diketonate precursors to form hybrid ALD/MLD materials. As the reactivity of the functional groups –OH, –NH₂ or –COOH is seen as a detachment of the proton, it is reasonable to study the acidity value pK_a of the precursors, found in Table 2 among some other known chemicals.¹²⁴ The pK_a is a negative logarithmic value ($\text{pK}_a = -\log_{10} K_a$) describing the proton donor affinity (Brønsted acidity) of a molecule, where the small pK_a (or large K_a) value indicates stronger proton donor affinity.

The high acidity or low pK_a of carboxylic acids can be explained by their affinity to form resonance-stabilized structures, where the extra electrons are relatively stable in the carboxylate (R-COO⁻) form.¹²⁴ The pK_a ballpark value for the reaction with different thd complexes is unknown.

Table 2. pK_a values (25°C in H₂O, first deprotonation) for some common substances and the organic molecules applied in this thesis, where the models for the molecules are not in scale.

Name	HCl	(COOH) ₂	TPA	CH ₃ -COOH	H(acac)	4-AP	HQ	H ₂ O ₂	H ₂ O
pK _a	-8	1.23	3.51	4.8	8.9	10.30	10.85	11.6	15.7



3.4.1 Case studies: Ca, Mn, Co and Cu based hybrid thin films

The goal for the hybrid studies was to find a way to use β -diketonate precursors to fabricate hybrid ALD/MLD thin films and moreover, to create novel transition metal hybrid thin films to expand the hybrid ALD/MLD materials catalogue. After realization of the high reactivity of the carboxylic acids, the studies were then conducted for six different β -diketonate precursors and two carboxylic acid precursors. Here the primary motivation was then to introduce the partially filled d-orbital species into the world of hybrid ALD/MLD materials and secondarily to investigate more on the +II oxidation state species with calcium. Some of the precursors are presented in Figure 20 and all the processes are described in Table 3.

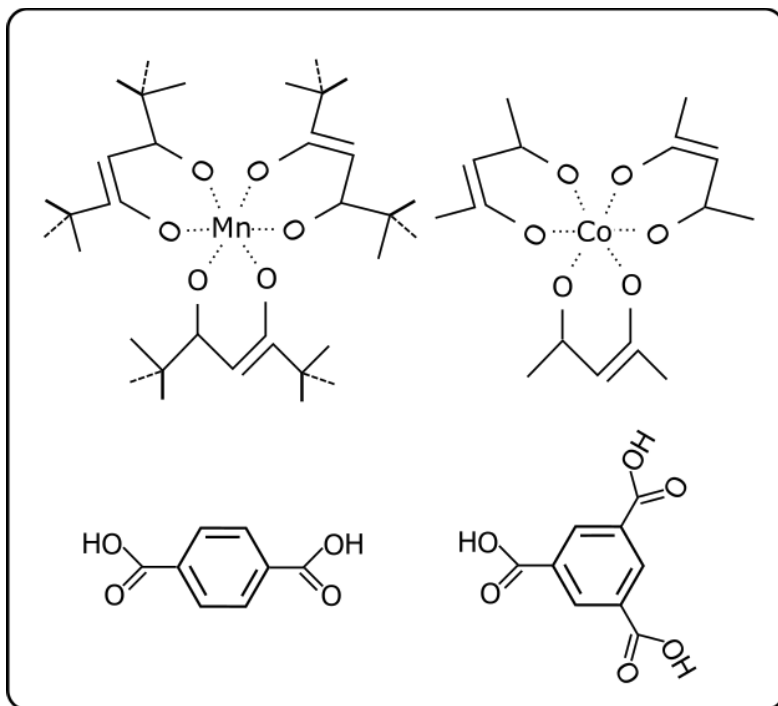


Figure 20. Examples of a few precursors applied in the thesis; $\text{Mn}(\text{thd})_3$, $\text{Co}(\text{acac})_3$, TPA and 1,3,5-BTC, proportions not to scale.

Table 3. The list of all ALD/MLD processes studied in this thesis.

#	Metal precursor	Organic precursor	Growth temp. [°C]	GPC [Å/c]	Crystalline?	Ref.
a	$\text{Ca}(\text{thd})_2$	1,3,5-BTC	220	6.5	No	-
b	$\text{Ca}(\text{thd})_2$	TPA	220	3.40	Yes	V
c*	$\text{Cu}(\text{acac})_2$	TPA	200	1.25	Yes	-
d*	$\text{Cu}(\text{thd})_2$	1,3,5-BTC	200	3.70	No	-
e	$\text{Cu}(\text{thd})_2$	TPA	200	1.38	Yes	III
f	$\text{Mn}(\text{thd})_3$	TPA	200	1.09	No	IV
g	$\text{Co}(\text{acac})_3$	TPA	200	1.10	No	IV
h	$\text{Co}(\text{thd})_2$	TPA	200	1.45	No	IV

*These processes were not optimized completely.

The pulse and purge data for the so-far studied processes show clear ALD type characteristics, where the metal precursor requires 2–5 s pulses and 2–5 s purges, and MLD precursors slightly longer 5–10 s and 10–15 s pulses and purges, respectively, shown in Figure 21. The pulse studies were conducted at 200°C for all except Calcium compounds, where 220°C was used due to the high sublimation temperature of $\text{Ca}(\text{thd})_2$ (190°C). Sublimation and growth temperatures were chosen to be as low as reasonably possible to study the low-

temperature growth of the films required i.e. for delicate substrates. The pulse and purge parameters were optimized in an experiment, where the hybrid ALD/MLD cycle was pre-guessed as 2–5 s ALD pulse \rightarrow 2 s N₂-purge \rightarrow 10 s MLD pulse \rightarrow 20 s N₂-purge, and then one parameter was changed at a time. Interpreting the pulse and purge studies of the so far studied materials it can be seen that ALD-type pulse patterns can be seen with each of the fully optimized processes. ALD-type purges are seen as well, except for Cu(thd)₂ + TPA process, where the ever-decreasing GPC value indicates of low sorption strength of the precursors.

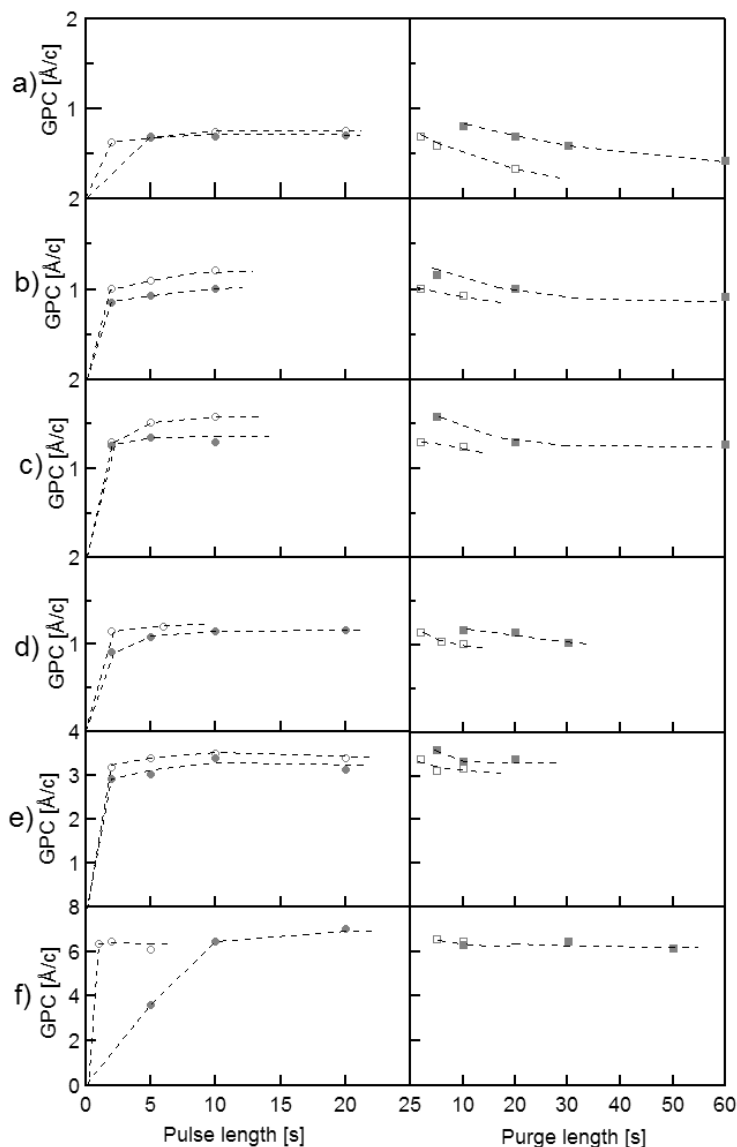


Figure 21. Pulse and purge data for the processes of a) Cu(thd)₂ + TPA, b) Mn(thd)₃ + TPA, c) Co(thd)₂ + TPA, d) Co(acac)₃ + TPA, e) Ca(thd)₂ + TPA and f) Ca(thd)₂ + 1,3,5-BTC. Inorganic and organic precursors are described with open and closed symbols, respectively.

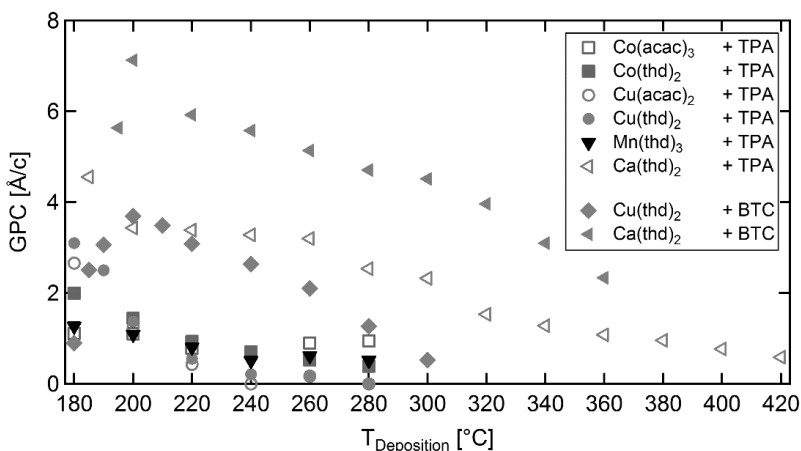


Figure 22. The growth windows for each ALD/MLD process listed in the table X.

The growth window studies (GPC vs. temperature) for each of the precursor combinations yielded visually similar graphs, where at low temperatures an increasing GPC value tops at 200–220 °C as 1–7 Å/c, and then declines steadily until the growth rate is either nonexistent or the inorganic precursor begins to decompose seen as yet again increasing GPC values in Figure 22. This type of GPC/temperature -behavior is typical for hybrid processes,¹⁰ and it is explained either by promotion of surface reactions due to initial diffusion of precursors into the film at medium temperatures until the increasing out-of-the-film desorption rate becomes more and more dominant at higher temperatures, or by the combined effect of thermal energy assisted reaction activation and the decrease of reactive sites at increasing temperatures.

The GPC values are less than calculated monolayer for each process, which is typical for ALD/MLD hybrid films, although it is not a definitive rule.^{10,125} The notably lower GPC values can occur for example due to tilting or double-reactions of the organic precursors or due to steric hindrance caused by the bulky ligands. The in-situ crystallizing materials Ca(thd)₂, Cu(acac)₂ and Cu(thd)₂ terephthalates grows faster (3.4 , 2.0 and 2.6 Å/c at 200, 190 and 190 °C, respectively) than their amorphous TPA counterparts (ca. 1.0 Å/c), which is explained by the ordered growth mechanisms as the crystalline structure forces the precursors to more upright positions. The copper or calcium + 1,3,5-BTC processes yield notably higher GPC values than the TPA-processes due to the bulkier ligand which is not as prone to triple reactions with the surface, thus should lead into sticking more vertically on the surface. The growth linearity experiments at 200–220 °C resulted in highly linear growth with R² values ranging from 0.997–0.999 for each process except copper–terephthalate (Cu-TP) films, which yielded 0.998 and 0.990 for acac and thd processes, respectively. The notably lower correlation factor for Cu(thd)₂–TPA process yielded from rough crystalline structure forming process combined with high temperature sensitivity, resulted in uneven and rough films near the phase-change region and TPA sublimation temperatures of 180–200 °C. Crystalline

Ca-TP films grows at higher temperatures with better controllability, and a linear increase in roughness with thickness was observed, explained by in-situ crystallization.^V

The crystalline ALD/MLD fabricated hybrid films themselves are not a completely novel phenomenon, as also a few zinc processes have been found recently.^{23–25} In addition to the crystalline hybrid films being quite rare, the notable aspect is that none of these previously reported processes have yielded crystalline structures without post-deposition processing of 1 or 2 extra steps. The one-step synthesis of thin crystalline films described in **III** and **V** makes the processing very simple and one order of magnitude faster compared to conventional layer-by-layer methods.¹²⁶ This does not include the superior prospect of the ALD/MLD method where the pre-fabrication of self-assembled monolayers (SAMs) are not required, since the film can be deposited directly on e.g. silicon, plastic or three-dimensional high-surface area structures.

The GIXRD patterns and the corresponding structures for Cu-TP and Ca-TP films are presented in Figures 23–27, where the two materials have completely different structures as Cu-TP forms a 2-dimensional paddlewheel structure,^{127–130} and Ca-TP a 3-dimensional cross-linked structure.^{131–135} In previous studies on Ca-TP, the bulk samples contain large amounts of solvents such as H₂O or DMF in the structure, while using ALD/MLD method the dry version is obtained immediately. For ALD/MLD fabricated Cu-TP MOF, the critical temperature where the structure forms is narrow, only 180–190 °C, while for Ca-TP, the crystalline structure forms from 190 °C to 420 °C. The upper limit of the depositions comes from the the pity of the scientist towards the 30-year-old reactor, its o-rings and glass parts.

The Cu-TP MOF film can adsorb and desorb H₂O molecules from air humidity, which can be seen in Figure 24(a), where GIXRD analysis was performed from as-deposited film (1), film rested for 8 days (2), film rested for 26 days (3), and after vacuum drying in different temperatures of 85 °C for 1 day (4), at 130 °C for 3 days (5), at 200 °C for 2 days (6), at 230 °C for 3 days (7) and at 260 °C for 2 days (8). The water adsorption is seen as the rise of certain peaks (ca. 8 °, 17 ° and 26 °) belonging to the ligand position filling with water. From

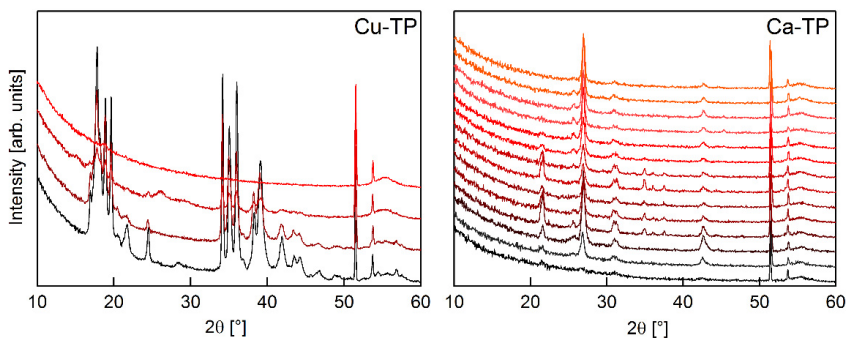


Figure 23. Crystallinity vs. deposition temperature. For Cu-TP on the left, the studied deposition temperatures were 180, 185, 195 and 200 °C from bottom to top and for Ca-TP on the right, 185, 190, 200 °C and then at 20 °C intervals up to 420 °C from bottom to top.

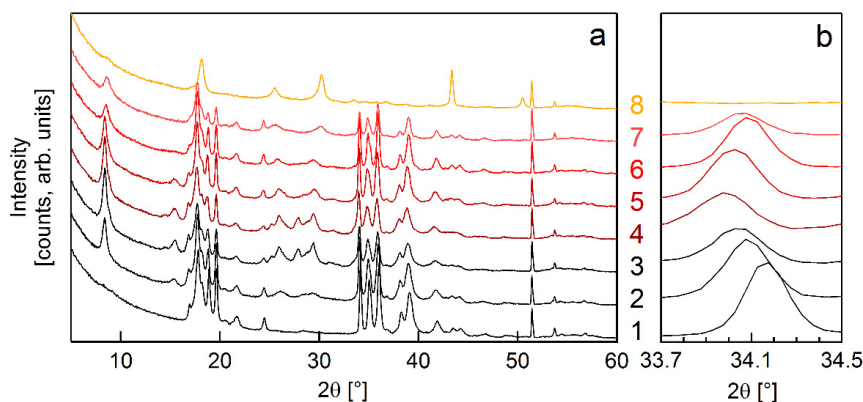


Figure 24. Cu-TP adsorbs moisture from air humidity and changes into wetted structure after 26 days of exposure to humid air. The original dry structure can be regenerated by heating the sample in vacuum. The graphs represent as deposited film (1), films rested for 8 days (2) and 26 days (3), films after vacuum drying in 85 °C (4), 130 °C (5), 200 °C (6), 230 °C (7) and 260 °C (8).

this regeneration analysis, it was found that the MOF desorbs the water molecules at ca. 200 °C in vacuum, while at ca. 230+ °C, the structure was found to be destroyed by thermal combustion, which in the same time might explain the lack of film growth at those temperatures. The Figure 24(b) shows how the (2 0 0) peak shifts into lower angle (=unit cell grows larger) as water is adsorbed and shifts back to its “dry” position as water is excluded from the structure, further proving the reversibility of the adsorption/desorption process. The water molecule is coordinated to the copper molecules on the side of the 2D-network, marked with “L” as a ligand spot in Figure 25.

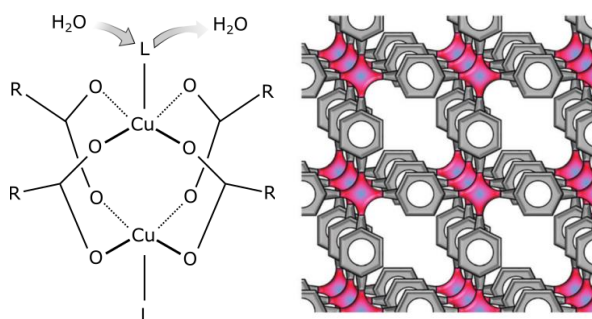


Figure 25. Visual interpretation of crystalline Cu-TP structure which forms a 2-dimensional network, where the R symbolizes the benzene ring of terephthalate. The adsorbed water molecules can attach into the ligand site marked with “L” symbol (left figure) or to the blue marked spots in the network figure (right).

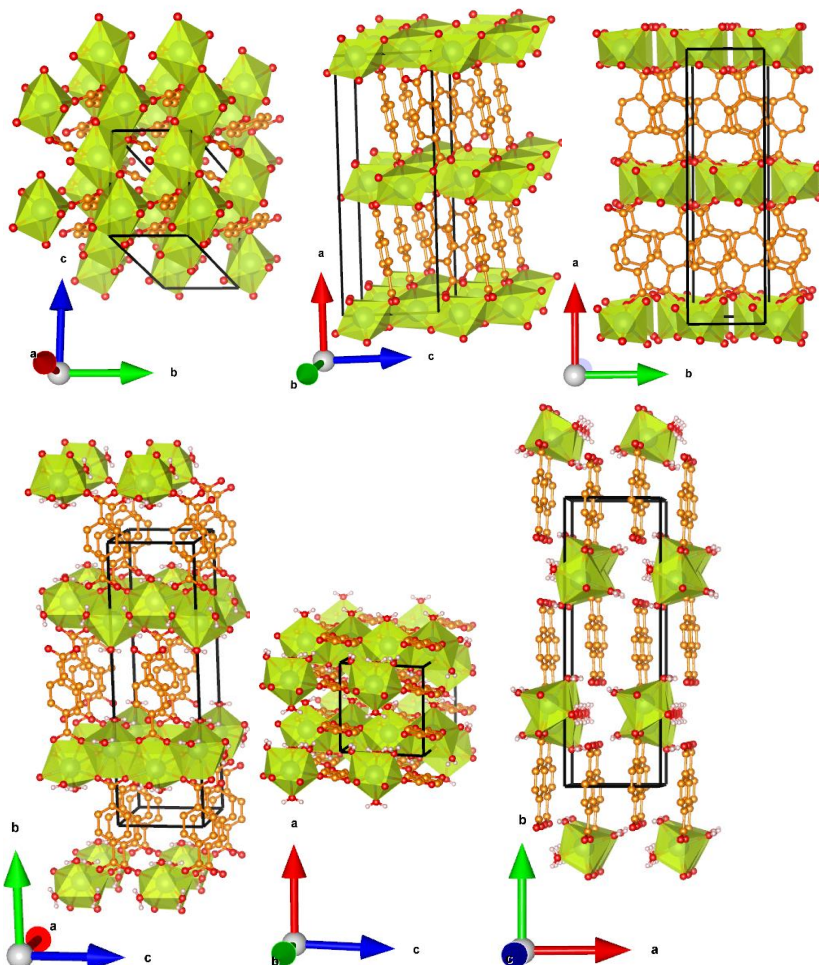


Figure 26. Visual interpretations of dry (top) and wetted (bottom) Ca-TP crystal structures from a, b and c axes (left, middle and right, respectively).

The Ca-TP structure can adsorb and desorb moisture as well but in here, the crystal structure changes drastically unlike in the Cu-TP case. The TP molecule detaches from its other end and forms a zipper-type structure where the calcium oxides and water molecules are at the same inorganic layer, and terephthalates are at separate layers, shown in Figure 26.

The water adsorption and desorption was monitored by the change of GIXRD patterns (see Fig. 27) measured in a scheme where at first, (a) the sample was measured immediately after deposition to obtain the dry structure, then (b) let to adsorb moisture for 90 days at room temperature in ca. 30% relative humidity conditions to completely wet the structure, (c) regenerated in 15 minutes of 100 °C under argon gas flow in RTA oven, tried to wet (d) at 30 % relative humidity over 24 hours and (e) over a decanter of water heated in a hotplate (55 °C) and then (f) regenerated at 80°C under argon gas flow at RTA. The low obtained regeneration temperatures are not in line with bulk material

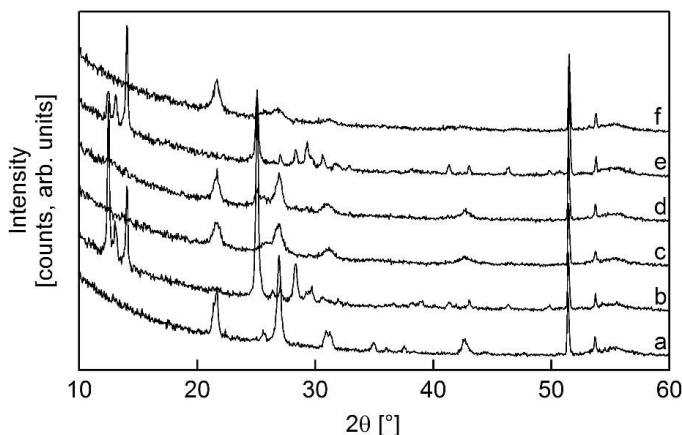


Figure 27. GIXRD patterns for the wetting and regeneration of the Ca-TP film. The graphs represent as-deposited film (a), film after 90 days (b), film after treatment in 100 °C (c), film after 1 day (d), film after water vapour treatment (e) and film after treatment in 80 °C (f).

studies, as there the sufficient regeneration temperature was estimated to be 400 °C interpreting the thermogravimetric data.¹³⁵

The chemical bonding in all the hybrid materials are similar, seen from the studies with FTIR method in Figure 28 below, where spectra of substrate (1, no film) and hybrid films yielded from processes of Mn(thd)₃ + TPA (2, 129 nm), Cu(thd)₂ + TPA (3, 84 nm), Cu(acac)₂ + TPA (4, 50 nm), Co(thd)₂ + TPA (5, 80 nm), Co(acac)₃ + TPA (6, 137 nm), Ca(thd)₂ + TPA (7, 98 nm, crystalline), Ca(thd)₂ + BTC (8, 89 nm) and Cu(thd)₂ + BTC (9, 87 nm) are shown. Absence of peaks at 1700-3500 cm⁻¹, indicates that the films are rather pure from H₂O, CO₂, RO-H, RN-H or RCOOH impurities. The signature area of 1250-1650 cm⁻¹ holds all the practical information in these hybrid structures where the benzene peaks can be seen at 1625 cm⁻¹ (aromatic C=C), 1435 cm⁻¹ (ring structure) and 1505 cm⁻¹ (aromatic C=C), C-O at 1310 cm⁻¹, the asymmetric and symmetric COO⁻ peaks at ca. 1580–1550 cm⁻¹ and 1395 cm⁻¹, respectively, indicate that all TP-films seem to have bridging type bonding for metal-to-carboxylates.^{III,IV,V}

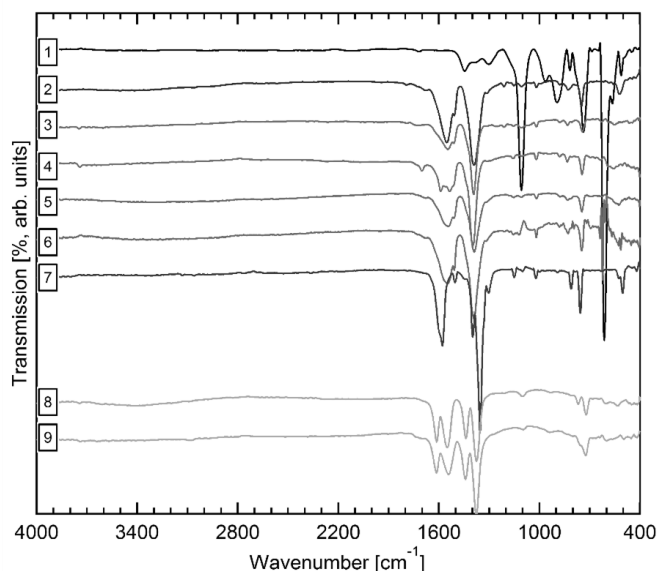


Figure 28. FTIR spectra of the substrate (1) and the hybrid thin films of Mn(thd)₃—TPA (2), Cu(thd)₂ + TPA (3), Cu(acac)₂ + TPA (4), Co(thd)₂ + TPA (5), Co(acac)₃ + TPA (6), Ca(thd)₂ + TPA (7), Cu(thd)₂ + BTC (8) and Cu(thd)₂ + BTC (9).

Since in this thesis work, both the deposition process characteristics (e.g. required pulse and purge lengths and temperature windows) and the basic thin film properties (e.g. bonding types from FTIR) were found to be essentially similar, it is difficult to evaluate the reason why some hybrid films are crystalline and some amorphous. More crystalline and amorphous hybrid ALD/MLD films are needed to prove any theories, but one approach could be to consider the coordination geometry of the metal cation in the precursor and in the formed/targeted crystalline structure.

XPS method was applied to verify the elemental composition of the amorphous and crystalline Cu-TP films, as the previously applied XRF or ICP-OES methods can not be used for these materials as the local equipment were not able to quantitatively detect carbon or oxygen. The results are presented in Table 4 below, where the metal-to-carbon and metal-to-oxygen ratios are presented and their corresponding ideal values from the crystal structure are in parentheses. The excess values of carbon and oxygen form roughly 2:1 ratio, which is the same ratio of carbon-to-oxygen in terephthalate, indicating possibly some extra TP/TPA-molecules on the surface region of the film. It is to be noted that each deposition was finished in hybrid pulse + purge. The XPS method was also applied to verify the oxidation state of the hybrid film obtained from Co(thd)₂—TPA process, as cobalt(II) has some tendency to oxidize into Co³⁺.¹³⁶ It was found^{IV} that the cobalt did retain, or at least mostly retained its oxidation state, proving that two different resulting cobalt hybrid films were deposited.

Table 4. XPS results for Cu-TP, amorphous and crystalline. Values for ideal structures are presented in parentheses.

Material	Crystallinity	T _{Deposition} [°C]	Metal-to-carbon	Metal-to-oxygen
Cu-TP	Amorphous	210 °C	1:14.1 (-)	1:6.6 (-)
Cu-TP	Crystalline	180 °C	1:10.1 (1:8)	1:4.8 (1:4)

The elongation properties of Ca-TP were investigated by depositing a relatively thick 420 nm hybrid ALD/MLD film over 25 μm thick Kapton plastic sheet, which is designed to endure ca. 300 °C temperatures and has decent elongation properties, shown in Figure 29(a). As the film thickness was just 1.65 % of the whole sample thickness, the resulting elongation profile was not suspected to have any notable changes or effects. However, it was found in Figure 29(b) that some of the samples had a small dent in their elongation profile at ca. 25% of elongation length.^v This dent was seen only in samples where the Ca-TP film was present, and in addition, where the Ca-TP film had been exposed to moisture for at least one full day. In “dry” Ca-TP films Figure 29(c), the dent was visible only when the more sensitive derivative-of-force was plotted instead of force to elongation, and they exhibited merely a ca. 1–2 % elongation resistance. In Figure 29 (bottom), scheme of the elongation process is proposed where the zipper-like structure assists the structure from breaking apart. This high elongation resistance seems unusual, as there must not be many crystalline inorganic-organic hybrid materials which have such feature.

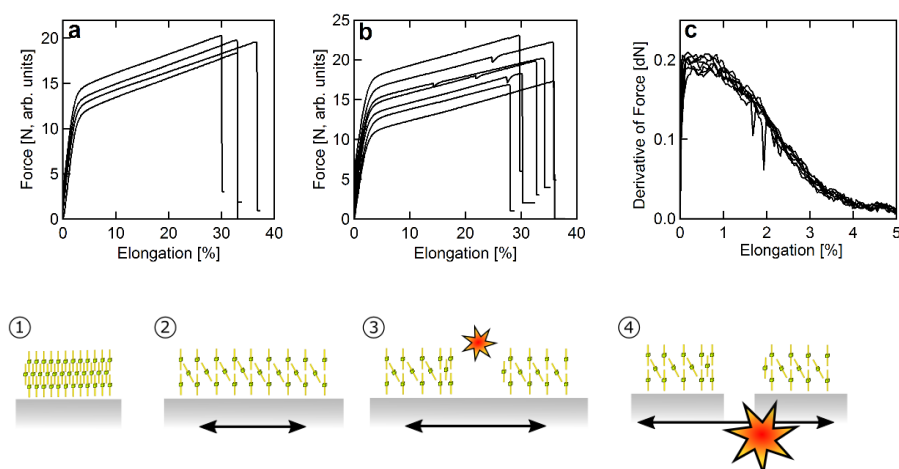


Figure 29. The elongation profiles of (a) four plain substrates and (b and c) seven Ca-TP films. The y-axes are force in graphs (a) and (b), while (c) has derivative of force for more precise data.

Finally, as the crystal structures in Figure 26 were thought of might having micropores to host small molecules, physisorption studies were applied to estimate the surface area of the Ca-TP. It was not known if the small sample sizes would be sufficient for the physisorption measurements, but after the analyses of three samples applying one BET and two NLDFT methods of a total sample sizes of 0.4703, 0.6318 and 0.7175 g, where most of the mass is obtained from silicon substrate rather than the 95.2–99.0 nm thick films, the surface area was calculated to be ca. $2500 \pm 500 \text{ m}^2/\text{g}$ from the non-rounded results of 2453, 2521 and 2575 m^2/g , respectively. The high error margin comes from the high uncertainty due to the ultra low mass of the samples. Measuring the plain silicon substrate gave 0 m^2/g result, which implies that all the results were obtained from the small amounts of the high-surface area thin films. The surface areas of thin film MOFs are have not been measured actively, which means that the obtained result is hard to compare to values from similar method, but as seen in the compilation by Farha *et al.*¹³⁷ for bulk materials, the obtained surface area could be logical as e.g. MOF from similar organic constituent of Zn-TP had surface area of 3800 m^2/g and 1.55 cm^3/g pore size. The distribution of pore sizes for high-surface area MOFs are 1.1–4.4 cm^3/g . The pore size analysis by the NLDFT method from two Ca-TP samples gave 4.1 and 4.2 cm^3/g results which are supposedly on the high-side.

4. Conclusions

Basic research on fundamental material properties can yield unexpected and innovative results, even though initially the application potential would be unknown. As seen in the past, many of the fascinating technologies and novel ideas are based on new enabling functional materials. The goal of the dissertation was to study the deposition of new thin film materials fabricated with the ALD and ALD/MLD methods, and study their material properties from both the physical and chemical point of views. This resulted in two complex oxide materials manufactured with the ALD method and eight hybrid materials with the ALD/MLD method.

Probably the best cathode material for IT-SOFC would be thin, high surface area $(\text{La,Sr})(\text{Co,Fe})\text{O}_{3-\delta}$ with precisely crafted A- and B-site cation substitutions. Certainly, the ALD technique could be the method of choice in the fabrication of the material with the required high standards. The dissertation's oxide material studies of $\text{SrCoO}_{3-\delta}$ and $(\text{La,Sr})\text{CoO}_{3-\delta}$ completed the constituent set for the high-performance cathode material $(\text{La,Sr})(\text{Co,Fe})\text{O}_{3-\delta}$, where only the cathode material itself is now left for fabrication. Control of the cation stoichiometry was achieved and proved for the quaternary oxide system. It was found that heat-treatment at ca. 600–700°C was required to crystallize the oxides, resulting in evacuation of the impurities from the structure. In addition, the studies yielded an idea for the effect of molar masses of the typical hydrocarbon-based ligands applicable as a tool for estimating the maximum growth per cycle value, which is particularly applicable with molar masses below ca. 200 g/mol, where the clumping of the material has not that large effect. This is particularly handy in cases where the substitution rate of a complex oxide is being optimized and the suitable precursors are sought.

The eight hybrid ALD/MLD processes covered in the thesis extended the family of available ALD/MLD materials from the previously commonly employed aluminium, zinc and titanium compounds to cover the partially filled d-orbital cations of manganese, cobalt and copper, which are known from their exciting magnetic and electrical application potential, and the alkaline earth metal calcium. The MLD precursors, TPA and 1,3,5-BTC were found to excel when paired with the β -diketonate type thd and acac precursors. The highly increased proton donation affinity of the carboxylic acids compared to hydroxyl or amine groups must be the main driving factor, but the actual reacting pKa limit remains unknown. Moreover, two new crystalline hybrid materials were

successfully fabricated with the ALD/MLD method, using fast and easy one-step procedure. In addition to their capability of reversibly adsorbing/desorbing gas molecules, the alkaline earth metal based hybrid material Ca-TP was found to exhibit outstanding elastic properties, where the unique zipper-type structure seems to be the key factor. Definitely, more material studies are required if the reason behind the crystalline hybrid film formation is pursued.

Recently a respectably growing number of ALD fabricated complex oxide and hybrid ALD/MLD thin film studies are seen from around the world, including the areas of high- κ insulators and water-splitting photocathodes. Some profoundly exciting materials have already been seen and trend is clear – complex thin films are here.

References

1. Suntola, T. & Antson, J. Method for producing compound thin films, US Pat. 4,058,430 (1977).
2. Koltsov, S. I., Kuznetsova, G. N. & Alekovskii, V. B. Study of the stoichiometry of the products formed in the reaction of trichlorosilane with the functional groups of polysilicic acid, *J. Appl. Chem. USSR* **40**, 2644 (1967).
3. Alekovskii, V. B. Chemistry and technology of solids. *J. Appl. Chem. USSR* **47**, 2207 (1974).
4. Leskelä, M. & Ritala, M. Atomic layer deposition chemistry: recent developments and future challenges, *Angew. Chem.* **42**, 5548–54 (2003).
5. George, S. M. Atomic layer deposition: an overview, *Chem. Rev.* **110**, 111–31 (2010).
6. Miikkulainen, V., Leskelä, M., Ritala, M. & Puurunen, R. L. Crystallinity of inorganic films grown by atomic layer deposition: Overview and general trends, *J. Appl. Phys.* **113**, 021301 (2013).
7. Hwang, C. S. & Yoo, C. Y. Atomic Layer Deposition for Semiconductors, *Springer* (2014).
8. McDaniel, M. D., Ngo, T. Q., Hu, S., Posadas, A., Demkov, A. A. & Ekerdt, J. G. Atomic layer deposition of perovskite oxides and their epitaxial integration with Si, Ge, and other semiconductors, *Appl. Phys. Rev.* **2**, 041301 (2015).
9. Bhalla, A., Guo, R. & Roy, R. The perovskite structure – a review of its role in ceramic science and technology, *Mater. Res. Innov.* 3–26 (2000).
10. Sundberg, P. & Karppinen, M. Organic and inorganic-organic thin film structures by molecular layer deposition: a review, *Beilstein J. Nanotechnol.* **5**, 1104–1136 (2014).
11. George, B. S. M. & Yoon, B. Molecular Layer Deposition of Organic and Hybrid Organic-Inorganic Polymers, *Mater. Matters* **3**, 34–37 (2008).
12. Johnson, R. W., Hultqvist, A. & Bent, S. F. A brief review of atomic layer deposition: From fundamentals to applications, *Mater. Today* **17**, 236–246 (2014).
13. Nisula, M. & Karppinen, M. Atomic/molecular layer deposition of lithium terephthalate thin films as high rate capability Li-ion battery anodes, *ACS Nano Lett.* **16**, 1276–1281 (2016).
14. Tanskanen, A. & Karppinen, M. Iron-based inorganic-organic hybrid and superlattice thin films by ALD/MLD, *Dalton Trans.* **44**, 19194–19199 (2015).
15. Giedraityte, Z., Sundberg, P. & Karppinen, M. Flexible inorganic-organic thin film phosphors by ALD/MLD, *J. Mater. Chem. C* **3**, 12316–12321 (2015).
16. Niemelä, J.-P., Karttunen, A. J. & Karppinen, M. Inorganic–organic superlattice thin films for thermoelectrics, *J. Mater. Chem. C* **3**, 10349–10361 (2015).
17. Tynell, T., Terasaki, I., Yamauchi, H. & Karppinen, M. Thermoelectric characteristics of (Zn,Al)O/hydroquinone superlattices, *J. Mater. Chem. A* **1**, 13619–13624 (2013).
18. Tynell, T., Giri, A., Gaskins, J., Hopkins, P. E., Mele, P., Miyazaki, K. & Karppinen, M. Efficiently suppressed thermal conductivity in ZnO thin films via periodic introduction of organic layers, *J. Mater. Chem. A* **2**, 12150–12152 (2014).

19. Venkatasubramanian, R., Siivola, E., Colpitts, T. & O'Quinn, B. Thin-film thermoelectric devices with high room-temperature figures of merit, *Nature* **413**, 597–602 (2001).
20. Vähä-Nissi, M., Sundberg, P., Kauppi, E., Hirvikorpi, T., Sievänen, J., Sood, A., Karppinen, M. & Harlin, A. Barrier properties of Al₂O₃ and alucone coatings and nanolaminates on flexible biopolymer films, *Thin Solid Films* **520**, 6780–6785 (2012).
21. Feng-Bo, S., Yu, D., Yong-Qiang, Y., Ping, C., Ya-Hui, D., Xiao, W., Dan, Y. & Kai-wen, X. Fabrication of tunable [Al₂O₃:Alucone] thin-film encapsulations for top-emitting organic light-emitting diodes with high performance optical and barrier properties, *Org. Electron.* **15**, 2546–2552 (2014).
22. Yu, D., Yang, Y. Q., Chen, Z., Tao, Y. & Liu, Y. F. Recent progress on thin-film encapsulation technologies for organic electronic devices. *Opt. Commun.* **362**, 43–49 (2016).
23. Stassen, I., Styles, M., Greci, G., Van Gorp, H., Vanderlinden, W., De Feyter, S., Falcaro, P., De Vos, D., Vereecken, P. & Ameloot, R. Chemical vapour deposition of zeolitic imidazolate framework thin films, *Nat. Mater.* **15**, 304–310 (2015).
24. Salmi, L. D., Heikkilä, M. J., Puukilainen, E., Sajavaara, T., Grosso, D. & Ritala, M. Studies on atomic layer deposition of MOF-5 thin films, *Microporous Mesoporous Mater.* **182**, 147–154 (2013).
25. Salmi, L. D., Heikkilä, M. J., Puukilainen, E., Ritala, M. & Sajavaara, T. Studies on atomic layer deposition of IRMOF-8 thin films, *J. Vac. Sci. Technol. A* **33**, 01A121 (2015).
26. Yasaka, M. X-ray thin-film measurement techniques. V. X-ray reflectivity measurement, *Rigaku J.* **26**, 1–9 (2010).
27. Holy, V., Pietsch, U. & Baumbach, T. High Resolution X-ray Scattering from Thin Films and Multilayers, *Springer* (1999).
28. Petty, M. C. Molecular electronics: from principles to practice, *John Wiley & Sons, Ltd.* (2008).
29. Holger, O. Magnetic structures and phase transitions in thin and ultrathin films of heavy lanthanide metals investigated by resonant magnetic x-ray scattering, *Freie Universität Berlin* (2004).
30. Als-Nielsen, J. The liquid vapour interface, *Zeitschrift für Phys. B - Condens. Matter* **61**, 411–414 (1985).
31. Neerincx, D. G. & Vink, T. J. Depth profiling of thin ITO films by grazing incidence X-ray diffraction, *Thin Solid Films* **278**, 12–17 (1996).
32. Gelfi, M., Bontempi, E., Roberti, R., Armelao, L. & Depero, L. E. Residual stress analysis of thin films and coatings through XRD² experiments, *Thin Solid Films* **450**, 143–147 (2004).
33. Huang, T. C. & Predecki, P. K. Grazing-incidence x-ray technique for surface, interface and thin-film analysis, *Denver X-ray conference on Applications of X-ray Analysis* (1997).
34. Toney, M. F. & Brennan, S. Observation of the effect of refraction on x rays diffracted in a grazing-incidence asymmetric Bragg geometry, *Phys. Rev. B* **39**, 7963–7966 (1989).
35. Stuart, B. Infrared spectroscopy: Fundamentals and applications, *John Wiley & Sons, Ltd.* (2004).
36. Atkins, P. & de Paula, J. Atkins' Physical Chemistry, *Oxford University Press* (2006).
37. Brunauer, S., Emmett, P. H. & Teller, E. Adsorption of Gases in Multimolecular Layers, *J. Am. Chem. Soc.* **60**, 309–319 (1938).
38. Sing, K. S. Characterization of porous materials: Past, present and future, *Colloids Surfaces A Physicochem. Eng. Asp.* **241**, 3–7 (2004).
39. Barrett, E. P., Joyner, L. G. & Halenda, P. P. The determination of pore volume and area distributions in porous substances I. Computations from nitrogen isotherms, *The volume and area distributions in porous substances* **73**, 373–380 (1951).

40. Sing, K. The use of nitrogen adsorption for the characterisation of porous materials, *Colloids Surfaces A Physicochem. Eng. Asp.* **187-188**, 3–9 (2001).
41. Lowell, S., Shields, J. E., Thomas, M. A. & Thommes, M. Characterization of porous solids and powders: surface area, pore size and density, *Springer Science & Business Media* (2004).
42. Landers, J., Gor, G. Y. & Neimark, A. V. Density functional theory methods for characterization of porous materials, *Colloids Surfaces A Physicochem. Eng. Asp.* **437**, 3–32 (2013).
43. Callister, Jr., W. D. & Rethwisch, D. G. Fundamentals of Materials Science and Engineering: An Integrated Approach, *John Wiley & Sons, Ltd.* (2012).
44. Mattox, D. Handbook of Physical Vapor Deposition (PVD), *Elsevier Ltd.* (2010).
45. Ohnishi, T., Shibuya, K., Yamamoto, T. & Lippmaa, M. Defects and transport in complex oxide thin films, *J. Appl. Phys.* **103**, 103703 (2008).
46. Ashfold, M. N. R., Claeysens, F., Fuge, G. M. & Henley, S. J. Pulsed laser ablation and deposition of thin films, *Chem. Soc. Rev.* **33**, 23–31 (2004).
47. Niu, X., Stagon, S. P., Huang, H., Baldwin, J. K. & Misra, A. Smallest metallic nanorods using physical vapor deposition, *Phys. Rev. Lett.* **110**, 1–5 (2013).
48. Robbie, K., Broer, D. & Brett, M. Chiral nematic order in liquid crystals imposed by an engineered inorganic nanostructure, *Nature* **399**, 764–766 (1999).
49. Robbie, K., Beydaghyan, G., Brown, T., Dean, C., Adams, J. & Buzea, C. Ultrahigh vacuum glancing angle deposition system for thin films with controlled three-dimensional nanoscale structure, *Rev. Sci. Instrum.* **75**, 1089–1097 (2004).
50. Pedersen, H. & Elliott, S. D. Studying chemical vapor deposition processes with theoretical chemistry, *Theor. Chem. Acc.* **133**, 1–10 (2014).
51. Parsons, G. N., George, S. M. & Knez, M. Progress and future directions for atomic layer deposition and ALD-based chemistry, *MRS Bull.* **36**, 865–871 (2011).
52. Groner, M. D., Fabreguette, F. H., Elam, J. W. & George, S. M. Low-Temperature Al₂O₃ Atomic Layer Deposition, *Chem. Mater.* **16**, 639–645 (2004).
53. Dameron, A. A., Seghete, D., Burton, B. B., Davidson, S. D., Cavanagh, A. S., Bertrand, J. A. & George, S. M. Molecular Layer Deposition of Alucone Polymer Films Using Trimethylaluminum and Ethylene Glycol, *Chem. Mater.* **20**, 3315–3326 (2008).
54. Puurunen, R. L. Surface chemistry of atomic layer deposition: A case study for the trimethylaluminum/water process, *J. Appl. Phys.* **97**, 121301 (2005).
55. Puurunen, R. L. & Vandervorst, W. Island growth as a growth mode in atomic layer deposition: A phenomenological model, *J. Appl. Phys.* **96**, 7686–7695 (2004).
56. Mack, J. F., Van Stockum, P. B., Yemane, Y. T., Logar, M., Iwadata, H. & Prinz, F. B. Observing the nucleation phase of atomic layer deposition in situ, *Chem. Mater.* **24**, 4357–4362 (2012).
57. Siimon, H. & Aarik, J. Thickness profiles of thin films caused by secondary reactions in flow-type atomic layer deposition reactors, *J. Phys. D: Appl. Phys.* **30**, 1725 (1997).
58. Kukli, K., Aarik, J., Ritala, M., Uustare, T., Sajavaara, T., Lu, J., Sundqvist, J., Aidla, A., Pung, L., Härsta, A. & Leskelä, M. Effect of selected atomic layer deposition parameters on the structure and dielectric properties of hafnium oxide films, *J. Appl. Phys.* **96**, 5298–5307 (2004).
59. Mäntymäki, M., Heikkilä, M. J., Puukilainen, E., Mizohata, K., Marchand, B., Räisänen, J., Ritala, M. & Leskelä, M. Atomic layer deposition of AlF₃ thin films using halide precursors, *Chem. Mater.* **27**, 604–611 (2015).

60. Kosola, A., Putkonen, M., Johansson, L.-S. & Niinistö, L. Effect of annealing in processing of strontium titanate thin films by ALD, *Appl. Surf. Sci.* **211**, 102–112 (2003).
61. Putkonen, M., Aaltonen, T., Alnes, M., Sajavaara, T., Nilsen, O. & Fjellvåg, H. Atomic layer deposition of lithium containing thin films, *J. Mater. Chem.* **19**, 8767 (2009).
62. Nieminen, M., Sajavaara, T., Rauhala, E., Putkonen, M. & Niinistö, L. Surface-controlled growth of LaAlO_3 thin films by atomic layer epitaxy, *J. Mater. Chem.* **11**, 2340–2345 (2001).
63. Myllymäki, P., Roeckerath, M., Lopes, J. M., Schubert, J., Mizohata, K., Putkonen, M. & Niinistö, L. Rare earth scandate thin films by atomic layer deposition: effect of the rare earth cation size, *J. Mater. Chem.* **20**, 4207–4212 (2010).
64. Ahvenniemi, E., Matvejeff, M. & Karppinen, M. Atomic layer deposition of quaternary oxide $(\text{La,Sr})\text{CoO}_{3-\delta}$ thin films, *Dalton Trans.* **44**, 8001–8006 (2015).
65. Seim, H., Nieminen, M., Niinistö, L. & Fjellvåg, H. Growth of LaCoO_3 thin films from β -diketonate precursors, *Appl. Surf. Sci.* **112**, 243–250 (1997).
66. Seim, H., Mölsä, H., Nieminen, M., Fjellvåg, H. & Niinistö, L. Deposition of LaNiO_3 thin films in an atomic layer epitaxy reactor, *J. Mater. Chem.* **7**, 449–454 (1997).
67. Huang, R. & Kitai, A. H. Preparation and characterization of thin films of MgO , Al_2O_3 and MgAl_2O_4 by atomic layer deposition, *J. Electron. Mater.* **22**, 215–220 (1993).
68. Lybeck, J., Valkeapää, M., Shibasaki, S., Terasaki, I., Yamauchi, H. & Karppinen, M. Thermoelectric Properties of Oxygen-Tuned ALD-Grown $[\text{Ca}_2\text{CoO}_3]_{0.62}[\text{CoO}_2]$ Thin Films, *Chem. Mater.* **22**, 5900–5904 (2010).
69. Vehkamäki, M., Ritala, M., Leskelä, M., Jones, A. C., Davies, H. O., Sajavaara, T. & Rauhala, E. Atomic Layer Deposition of Strontium Tantalate Thin Films from Bimetallic Precursors and Water, *J. Electrochem. Soc.* **151**, F69–F72 (2004).
70. Vehkamäki, M. & Hatanpää, T. Bismuth precursors for atomic layer deposition of bismuth-containing oxide films, *J. Mater. Chem.* **14**, 3191–3197 (2004).
71. Watanabe, T. & Hoffmann-Eifert, S. Liquid injection atomic layer deposition of $\text{Pb}(\text{Zr,Ti})\text{O}_3$ thin films on three dimensional structures, Applications of Ferroelectrics (2007).
72. Nilsen, O., Rauwel, E., Fjellvåg, H. & Kjekshus, A. Growth of $\text{La}_{1-x}\text{Ca}_x\text{MnO}_3$ thin films by atomic layer deposition, *J. Mater. Chem.* **17**, 1466–1475 (2007).
73. Lie, M., Nilsen, O., Fjellvåg, H. & Kjekshus, A. Growth of $\text{La}_{1-x}\text{Sr}_x\text{FeO}_3$ thin films by atomic layer deposition, *Dalton Trans.* **3**, 481–489 (2009).
74. Holme, T. P., Lee, C. & Prinz, F. B. Atomic layer deposition of LSM cathodes for solid oxide fuel cells, *Solid State Ionics* **179**, 1540–1544 (2008).
75. Muneshwar, T. & Cadien, K. AxBAxB... pulsed atomic layer deposition: Numerical growth model and experiments, *J. Appl. Phys.* **119**, 085306 (2016).
76. Elam, J. W. & George, S. M. Growth of $\text{ZnO}/\text{Al}_2\text{O}_3$ alloy films using atomic layer deposition techniques, *Chem. Mater.* **15**, 1020–1028 (2003).
77. Vehkamäki, M., Hatanpää, T., Hänninen, T., Ritala, M. & Leskelä, M. Growth of SrTiO_3 and BaTiO_3 thin films by atomic layer deposition, *Electrochem. Solid-state Lett.* **2**, 504–506 (1999).
78. Elliott, S. & Nilsen, O. (Invited) Reaction Mechanisms in ALD of Ternary Oxides, *ECS Trans.* **41**, 175–183 (2011).
79. Ritala, M., Leskelä, M. & Rauhala, E. Atomic Layer Epitaxy Growth of Titanium Dioxide Thin Films from Titanium Ethoxide, *Chem. Mater.* **6**, 556–561 (1994).
80. Ritala, M., Leskelä, M., Niinistö, L. & Haussalo, P. Titanium Isopropoxide as a Precursor in Atomic Layer Epitaxy of Titanium Dioxide Thin Films, *Chem. Mater.* **5**, 1174–1181 (1993).

81. Ylilammi, M. Monolayer thickness in atomic layer deposition, *Thin Solid Films* **279**, 124–130 (1996).
82. Lowell, S. & Shields, J. E. Powder surface area and porosity, *Chapman & Hall* (1998).
83. Hall, P. G. & Stoeckli, H. F. Adsorption of Nitrogen, n-Butane and neo-Pentane on Chloro-Hydrocarbon Polymers, *Trans. Faraday Soc.* **65**, 3334–3340 (1969).
84. Brett, D. J. L., Atkinson, A., Brandon, N. P. & Skinner, S. J. Intermediate temperature solid oxide fuel cells, *Chem. Soc. Rev.* **37**, 1568–78 (2008).
85. Steele, B. C. & Heinzel, A. Materials for fuel-cell technologies, *Nature* **414**, 345–52 (2001).
86. Beckel, D., Bieberle-Hütter, A., Harvey, A., Infortuna, A., Muecke, U. P., Prestat, M., Rupp, J. L. M. & Gauckler, L. J. Thin films for micro solid oxide fuel cells, *J. Power Sources* **173**, 325–345 (2007).
87. Ralph, J. M., Schoeler, A. C. & Krumpelt, M. Materials for lower temperature solid oxide fuel cells, *J. Mater. Sci.* **36**, 1161–1172 (2001).
88. Prestat, M., Infortuna, A., Korrodi, S., Rey-Mermet, S., Murali, P. & Gauckler, L. J. Oxygen reduction at thin dense $\text{La}_{0.52}\text{Sr}_{0.48}\text{Co}_{0.18}\text{Fe}_{0.82}\text{O}_{3-\delta}$ electrodes, *J. Electroceramics* **18**, 111–120 (2007).
89. Endo, A., Wada, S., Wen, C., Komlyama, H. & Yamada, K. Low Overvoltage Mechanism of High Ionic Conducting Cathode for Solid Oxide Fuel Cell, *J. Electrochem. Soc.* **145**, 1997–1999 (1998).
90. Peters, C., Weber, A. & Ivers-Tiffe'e, E. Nanoscaled $(\text{La}_{0.5}\text{Sr}_{0.5})\text{CoO}_{3-\delta}$ Thin Film Cathodes for SOFC Application at $500^\circ\text{C} < T < 700^\circ\text{C}$, *J. Electrochem. Soc.* **155**, B730–B737 (2008).
91. Wang, S., Yoon, J., Huang, D., Wang, H. & Jacobson, A. J. Electrochemical Properties of Nanocrystalline $\text{La}_{0.5}\text{Sr}_{0.5}\text{CoO}_{3-x}$ Thin Films, *Chem. Mater.* **22**, 776–782 (2010).
92. Wachsman, E. D. & Lee, K. T. Lowering the temperature of solid oxide fuel cells, *Science* **334**, 935–939 (2011).
93. Sun, C., Hui, R. & Roller, J. Cathode materials for solid oxide fuel cells: a review, *J. Solid State Electrochem.* **14**, 1125–1144 (2009).
94. Jacobson, A. J. Materials for Solid Oxide Fuel Cells, *Chem. Mater.* **22**, 660–674 (2010).
95. Ahvenniemi, E., Matvejeff, M. & Karppinen, M. $\text{SrCoO}_{3-\delta}$ thin films by atomic layer deposition, *Appl. Surf. Sci.* **320**, 838–842 (2014).
96. Hammond, G. S., Nonhebel, D. C. & Wu, C.-H. S. Chelates of β -Diketones. V. Preparation and Properties of Chelates Containing Sterically Hindered Ligands, *Inorg. Chem.* **2**, 73–76 (1963).
97. Mineshige, A., Kobune, M., Fujii, S., Ogumi, Z. & Inaba, M. Metal-Insulator Transition and Crystal Structure of $\text{La}_{1-x}\text{Sr}_x\text{CoO}_3$ as Functions of Sr-Content, Temperature, and Oxygen Partial Pressure, *J. Solid State Chem.* **142**, 374–381 (1999).
98. Iwasaki, K., Ito, T., Nagasaki, T., Arita, Y., Yoshino, M. & Matsui, T. Thermoelectric properties of polycrystalline $\text{La}_{1-x}\text{Sr}_x\text{CoO}_3$, *J. Solid State Chem.* **181**, 3145–3150 (2008).
99. Kozuka, H., Yamada, H., Hishida, T., Yamagiwa, K., Ohbayashi, K. & Koumoto, K. Electronic transport properties of the perovskite-type oxides $\text{La}_{1-x}\text{Sr}_x\text{CoO}_{3\pm\delta}$, *J. Mater. Chem.* **22**, 20217 (2012).
100. Matvejeff, M., Ahvenniemi, E., Takahashi, R. & Lippmaa, M. Magnetic coupling at perovskite and rock-salt structured interfaces, *Appl. Phys. Lett.* **107**, (2015).
101. Iwasaki, K., Ito, T., Matsui, T., Nagasaki, T., Ohta, S. & Koumoto, K. Synthesis of an oxygen nonstoichiometric $\text{Sr}_6\text{Co}_5\text{O}_{15}$ phase, *Mater. Res. Bull.* **41**, 732–739 (2006).
102. Harrison, W. T. A., Hegwood, S. L. & Jacobson, A. J. A powder neutron diffraction determination of the structure of $\text{Sr}_6\text{Co}_5\text{O}_{15}$, formerly described as the low-temperature hexagonal form of SrCoO_{3-x} , *J. Chem. Soc. Chem. Commun.* 1953–1954 (1995).

103. Iwasaki, K., Shimada, M., Yamane, H., Takahashi, J., Kubota, S., Nagasaki, T., Arita, Y., Yuhara, J., Nishi, Y. & Matsui, T. Electrical resistivity and Seebeck coefficient of $\text{Sr}_6\text{Co}_5\text{O}_{15}$, *J. Alloys Compd.* **377**, 272–276 (2004).
104. van Doorn, R. H. E. & Burggraaf, A. J. Structural aspects of the ionic conductivity of $\text{La}_{1-x}\text{Sr}_x\text{CoO}_{3-d}$, *Solid State Ionics* **128**, 65–78 (2000).
105. Yoshimura, T., Tatsuura, S. & Sotoyama, W. Polymer films formed with monolayer growth steps by molecular layer deposition, *Appl. Phys. Lett.* **59**, 482–484 (1991).
106. Yoshimura, T., Tatsuura, S., Sotoyama, W., Matsuura, A. & Hayano, T. Quantum wire and dot formation by chemical vapor deposition and molecular layer deposition of one-dimensional conjugated polymer, *Appl. Phys. Lett.* **60**, 268–270 (1992).
107. Ivanova, T. V., Maydannik, P. S. & Cameron, D. C. Molecular layer deposition of polyethylene terephthalate thin films, *J. Vac. Sci. Technol. A* **30**, 01A121 (2012).
108. Adamczyk, N. M., Dameron, A. A. & George, S. M. Molecular Layer Deposition of Poly (p-phenylene terephthalamide) Films Using Terephthaloyl Chloride and p-Phenylenediamine, *Langmuir* **24**, 2081–2089 (2008).
109. Yoshimura, T. Molecular Layer Deposition (MLD): Monomolecular-Step Growth of Polymers with Designated Sequences, *Macromol. Symp.* **361**, 141–148 (2016).
110. Dresselhaus, M. S. Nanostructures and energy conversion, Rohsenow Symposium on Future Trends of Heat Transfer (2003).
111. Dresselhaus, M. S., Chen, G., Tang, M. Y., Yang, R., Lee, H., Wang, D., Ren, Z., Fleurial, J.-P. & Gogna, P. New Directions for Low-Dimensional Thermoelectric Materials, *Adv. Mater.* **19**, 1043–1053 (2007).
112. Furukawa, H., Cordova, K. E., O’Keeffe, M. & Yaghi, O. M. The chemistry and applications of metal-organic frameworks, *Science* **341**, 1230444 (2013).
113. Lee, J., Farha, O. K., Roberts, J., Scheidt, K. A., Nguyen, S. T. & Hupp, J. T. Metal-organic framework materials as catalysts, *Chem. Soc. Rev.* **38**, 1450–1459 (2009).
114. Horcajada, P., Serre, C., Maurin, G., Ramsahye, N. A., Balas, F., Vallet-Regí, M., Sebban, M., Taulelle, F. & Férey, G. Flexible porous metal-organic frameworks for a controlled drug delivery, *J. Am. Chem. Soc.* **130**, 6774–6780 (2008).
115. Han, S., Wei, Y., Valente, C. & Gassensmith, J. J. Chromatography in a Single Metal-Organic Framework (MOF) Crystal, *J. Am. Chem. Soc.* **132**, 16358–16361 (2010).
116. Liu, B. Metal-organic framework-based devices: separation and sensors, *J. Mater. Chem.* **22**, 10094–10101 (2012).
117. Nisula, M., Shindo, Y., Koga, H. & Karppinen, M. Atomic Layer Deposition of Lithium Phosphorus Oxynitride, *Chem. Mater.* **27**, 6987–6993 (2015).
118. Haas, K. H., Amberg-Schwab, S., Rose, K. & Schottner, G. Functionalized coatings based on inorganic-organic polymers (ORMOCERS) and their combination with vapor deposited inorganic thin films, *Surf. Coatings Technol.* **111**, 72–79 (1999).
119. Klepper, K. B., Nilsen, O., Francis, S. & Fjellvåg, H. Guidance of growth mode and structural character in organic-inorganic hybrid materials - a comparative study, *Dalton Trans.* **43**, 3492 (2014).
120. Nilsen, O., Klepper, K. B., Nielsen, H. & Fjellvåg, H. Deposition of Organic-Inorganic Hybrid Materials by Atomic Layer Deposition, *ECS Trans.* **16**, 3–14 (2008).
121. Klepper, K. B., Nilsen, O., Levy, T. & Fjellvåg, H. Atomic layer deposition of organic-inorganic hybrid materials based on unsaturated linear carboxylic acids, *Eur. J. Inorg. Chem.* **40**, 5305–5312 (2011).
122. Klepper, K. B., Nilsen, O., Hansen, P.-A. & Fjellvåg, H. Atomic layer deposition of organic-inorganic hybrid materials based on saturated linear carboxylic acids, *Dalton Trans.* **40**, 4636–4646 (2011).

123. Klepper, K. B., Nilsen, O. & Fjellvåg, H. Deposition of thin films of organic-inorganic hybrid materials based on aromatic carboxylic acids by atomic layer deposition, *Dalton Trans.* **39**, 11628–11635 (2010).
124. Jones, M. J. Organic chemistry, *W. W. Norton & Company Ltd.* (2005).
125. Sundberg, P. & Karppinen, M. Organic-inorganic thin films from TiCl_4 and 4-aminophenol precursors: A model case of ALD/MLD hybrid-material growth? *Eur. J. Inorg. Chem.* 968–974 (2014).
126. Shekhah, O., Liu, J., Fischer, R. A. & Wöll, C. MOF thin films: existing and future applications, *Chem. Soc. Rev.* **40**, 1081–1106 (2011).
127. Kumagai, H., Akita-Tanaka, M., Inoue, K., Takahashi, K., Kobayashi, H., Vilminot, S. & Kurmoo, M. Metal-Organic Frameworks from Copper Dimers with cis- and trans-1,4-cyclohexandicarboxylate and cis, cis-1,3,5-cyclohexanetricarboxylate, *Inorg. Chem.* **46**, 5949–5956 (2007).
128. Carson, C. G., Hardcastle, K., Schwartz, J., Liu, X., Hoffmann, C., Gerhardt, R. A. & Tannenbaum, R. Synthesis and structure characterization of copper terephthalate metal-organic frameworks, *Eur. J. Inorg. Chem.* 2338–2343 (2009).
129. Adams, R., Carson, C., Ward, J., Tannenbaum, R. & Koros, W. Metal organic framework mixed matrix membranes for gas separations, *Microporous Mesoporous Mater.* **131**, 13–20 (2010).
130. Liu, J., Shekhah, O., Arslan, H. K., Weidler, P., Gliemann, H., Bräse, S., Grosjean, S., Godt, A., Feng, X., Müllen, K., Magdau, I.-B., Heine, T. & Wöll, C. A novel series of isoreticular metal organic frameworks: realizing meta-stable structures by liquid phase epitaxy, *Sci. Rep.* **2**, 921 (2012).
131. Wang, L., Mou, C., Sun, Y., Liu, W., Deng, Q. & Li, J. Structure-property of metal organic frameworks calcium terephthalates anodes for lithium-ion batteries, *Electrochim. Acta* **173**, 235–241 (2015).
132. Zhang, X., Huang, Y. Y., Zhang, M. J., Zhang, J. & Yao, Y. G. A series of Ca(II) or Ba(II) inorganic-organic hybrid frameworks based on aromatic polycarboxylate ligands with the inorganic M-O-M (M = Ca, Ba) connectivity from 1D to 3D, *Cryst. Growth Des.* **12**, 3231–3238 (2012).
133. Liang, P.-C., Liu, H.-K., Yeh, C.-T., Lin, C.-H. & Zima, V. Supramolecular assembly of calcium metal-organic frameworks with structural transformations, *Cryst. Growth Des.* **11**, 699–708 (2011).
134. Panasyuk, G. P., Azarova, L. A., Khaddaj, M., Budova, G. P., Voroshilov, I. L., Grusha, T. V. & Izotov, A. D. Preparation and properties of sodium, potassium, magnesium, calcium, and aluminum terephthalates, *Inorg. Mater.* **39**, 1292–1297 (2003).
135. Mazaj, M., Mali, G., Rangus, M., Žunkovič, E., Kaučič, V. & Logar, N. Z. Spectroscopic studies of structural dynamics induced by heating and hydration: a case of calcium terephthalate metal organic framework, *J. Phys. Chem. C* **117**, 7552–7564 (2013).
136. Biesinger, M. C., Payne, B. P., Grosvenor, A. P., Lau, L. W. M., Gerson, A. R. & Smart, R. S. C. Resolving surface chemical states in XPS analysis of first row transition metals, oxides and hydroxides: Cr, Mn, Fe, Co and Ni, *Appl. Surf. Sci.* **257**, 2717–2730 (2011).
137. Farha, O. K., Eryazici, I., Jeong, N. C., Hauser, B. G., Wilmer, C. E., Sarjeant, A. A., Snurr, R. Q., Nguyen, S. T., Yazaydin, A. Ö. & Hupp, J. T. Metal-organic framework materials with ultrahigh surface areas: is the sky the limit? *J. Am. Chem. Soc.* **134**, 15016–15021 (2012).



ISBN 978-952-60-7080-3 (printed)
ISBN 978-952-60-7079-7 (pdf)
ISSN-L 1799-4934
ISSN 1799-4934 (printed)
ISSN 1799-4942 (pdf)

Aalto University
School of Chemical Technology
Department of Chemistry
www.aalto.fi

**BUSINESS +
ECONOMY**

**ART +
DESIGN +
ARCHITECTURE**

**SCIENCE +
TECHNOLOGY**

CROSSOVER

**DOCTORAL
DISSERTATIONS**